

# A NOVEL FAST ITERATIVE MOMENT METHOD FOR NEAR-CONTINUUM FLOWS \*

GUANGHAN LI , CHUNWU WANG , AND ZHICHENG HU †

**Abstract.** We develop a novel fast iterative moment method for the steady-state simulation of near-continuum flows, which are modeled by the high-order moment system derived from the Boltzmann-BGK equation. The fast convergence of the present method is mainly achieved by alternately solving the moment system and the hydrodynamic equations with consistent constitutive relations and boundary conditions. To be specific, the consistent hydrodynamic equations are solved in each alternating iteration to obtain improved predictions of macroscopic quantities, which are subsequently utilized to expedite the evolution of the moment system. Additionally, a semi-implicit scheme treating the collision term implicitly is introduced for the moment system. The resulting alternating iteration can be further accelerated by employing the Gauss-Seidel method with a cell-by-cell sweeping strategy. It is also noteworthy that such an alternating iteration works well with the nonlinear multigrid method. Numerical experiments for planar Couette flow, shock structure, and lid-driven cavity flow are carried out to investigate the performance of the proposed fast iterative moment method. All results show impressive efficiency and robustness.

**Key words.** Boltzmann-BGK equation, moment method, alternating iteration, fast convergence, near-continuum flow

**MSC codes.** 76P05, 65B99, 65M55

**1. Introduction.** The rarefaction of gas flow is usually measured by the Knudsen number  $Kn$ , defined as the ratio of the molecular mean free path to the characteristic flow length. According to its magnitude, gas flows are classified into four regimes [27]: continuum for  $Kn < 0.001$ , near-continuum or slip for  $0.001 < Kn < 0.1$ , transition for  $0.1 < Kn < 10$ , and free-molecular for  $Kn > 10$ . In the continuum flow regime, classical hydrodynamic equations such as the Navier-Stokes-Fourier (NSF) equations are sufficient to describe flow behavior accurately, whereas in other regimes, they gradually become inaccurate and may even break down, as rarefaction effects strengthen with increasing  $Kn$ . In this context, the Boltzmann equation, which is the fundamental equation of gas kinetic theory and widely considered valid across all flow regimes, serves as a necessary model for capturing rarefaction effects. However, solving the Boltzmann equation poses great computational challenges, due to its intrinsic high dimensional and nonlinear integro-differential structure. To balance accuracy and efficiency, a common strategy in the near-continuum flow regime replaces the complex binary collision integral with a simple relaxation term, such as the Bhatnagar-Gross-Krook (BGK) model [2]. Nevertheless, even with this simplification, numerical simulations can still be computationally expensive, especially for steady-state problems. Over the past few decades, considerable efforts have been devoted to developing efficient numerical methods for the Boltzmann-BGK equation, see, e.g., [23, 28, 10, 30, 4].

An attractive approach to reducing computational complexity is to apply model reduction techniques to yield macroscopic transport models, often referred to as extended hydrodynamic equations, which can capture non-negligible rarefaction effects beyond the capability of classical hydrodynamic equations [24]. Grad's moment method [16] is one of the most prominent techniques in this direction. It approximates the distribution function in the Boltzmann equation by a truncated series of Hermite functions, resulting in a high-order moment system, which, however, may suffer from ill-posedness and numerical difficulties due to the lack of hyperbolicity. Building upon this method, a class of globally hyperbolic regularized moment systems of arbitrary order has been systematically developed in recent years [8, 9]. Accompanying these systems, a unified numerical framework has been introduced and refined in [10, 11, 12]. This framework enables the tractable and efficient numerical implementation of high-order moment systems without the need to explicitly write out each moment equation, thereby facilitating the practical application of such models to a wide range of flow problems.

Steady-state solutions are of particular importance in many applications involving rarefied gas dynamics

---

\*Corresponding author: Zhicheng Hu. Submitted to the editors *July 30, 2025*.

**Funding:** This work was partially supported by the National Natural Science Foundation of China, No. 12171240, the National Science and Technology Major Project, No. J2019-II-0007-0027, the China Scholarship Council (CSC) under Grant No. 202406830048 and No. 202406830103, the Nanjing University of Aeronautics and Astronautics PhD short-term visiting scholar project, No. 230901DF08, and Postgraduate Research & Practice Innovation Program of Jiangsu Province, No. KYCX24\_0523. The computational resources were supported by High Performance Computing Platform of Nanjing University of Aeronautics and Astronautics, China.

†School of Mathematics, Nanjing University of Aeronautics and Astronautics, Nanjing 211106, China; Key Laboratory of Mathematical Modelling and High Performance Computing of Air Vehicles (NUAA), MIIT, Nanjing 211106, China.

*Email addresses:* liguanghai@nuaa.edu.cn (G. Li); wangcw@nuaa.edu.cn (C. Wang); huzhicheng@nuaa.edu.cn (Z. Hu).

and related non-equilibrium phenomena. Conventional numerical methods based on time integration typically require the solution to evolve over a prolonged period to reach steady state, leading to excessively high computational cost, especially in the near-continuum flow regime, where their convergence deteriorates significantly as  $Kn$  decreases. To address this efficiency bottleneck, attention has increasingly focused on specific solvers that bypass transient dynamics and accelerate convergence by directly targeting the steady-state solution. Among various acceleration strategies, multigrid methods [5, 26] have proven to be effective by employing coarse level corrections to efficiently eliminate error components across different scale levels.

Incorporating the nonlinear multigrid (NMG) method into the unified numerical framework of hyperbolic moment systems, we have developed an NMG solver based on spatial coarse grid corrections [20, 19], and a nonlinear multi-level moment (NMLM) solver based on lower-order model corrections [21, 18], which can also be interpreted as coarse level corrections in velocity space. Both solvers have shown notable efficiency gains compared to their single level counterparts. Nevertheless, as with time-integration-based single level solvers, their convergence for near-continuum flows still deteriorates markedly as  $Kn$  decreases, thereby weakening the acceleration effect. Moreover, while each method performs well individually, integrating both types of coarse level corrections to develop a more efficient multi-level solver remains nontrivial. Past attempts in this direction often encountered issues related to algorithmic stability and computational overhead. A robust integration strategy has yet to be established.

Inspired by the effectiveness of the NMLM solver, we propose in this paper a fast iterative moment (FIM) method that utilizes lower-order model corrections in a novel and more robust approach. To this end, we first note that the hydrodynamic equations are included in the moment system of order  $M \geq 2$ , and are expected to provide reasonably reliable predictions of the primary macroscopic quantities, namely density, mean velocity, and temperature, in the near-continuum flow regime. In contrast, higher-order moments tend to evolve more slowly and often remain small in this regime. Leveraging this inherent multi-scale structure, we then introduce the FIM framework, in which the high-order moment system and the hydrodynamic equations are solved alternately, with appropriate constitutive relations and boundary conditions to ensure consistency. Since the hydrodynamic equations therein effectively serve as the lower-order model to efficiently predict the primary macroscopic quantities, the FIM method can be interpreted as a restructured two-level NMLM method, offering significantly improved robustness and efficiency, particularly at smaller  $Kn$ . This enables efficient simulation even for moment systems of moderately large order. Additionally, the present FIM method shares conceptual similarities with the recently developed GSIS [25, 32], UGKS [33], and several other micro-macro acceleration methods [15, 7, 22, 30].

The FIM method is further improved by incorporating several additional acceleration strategies. Specifically, an implicit treatment of the collision term is introduced to enhance numerical stability in the small  $Kn$  regime. Meanwhile, a symmetric Gauss-Seidel method with a cell-by-cell sweeping strategy is applied to both the moment system and the hydrodynamic equations to accelerate convergence. In combination with these favorable strategies, a family of FIM solvers is developed, exhibiting enhanced performance. Moreover, these solvers can be readily integrated into the spatial NMG framework to achieve further acceleration. The resulting FIM-based NMG solver partially addresses the challenge of developing integrated multi-level solvers that leverage coarse level corrections in both spatial and velocity spaces.

The remainder of this paper is organized as follows. In section 2, we provide the necessary preliminaries, including the fundamental model, i.e., the Boltzmann-BGK equation, and its full discretization within the unified numerical framework of moment methods. The core framework of the FIM method is described in detail in section 3, while section 4 introduces additional targeted strategies, including the implicit treatment of the collision term, the symmetric Gauss-Seidel method, and the NMG method. Numerical experiments are presented in section 5 to investigate the performance of the proposed FIM and FIM-based NMG solvers. Finally, a brief conclusion is provided in section 6.

**2. Preliminaries.** In this section, we provide a brief overview of the governing Boltzmann-BGK equation and its moment system of arbitrary order, followed by a unified spatial discretization and a basic time integration scheme, namely the forward Euler method.

**2.1. Boltzmann-BGK equation.** In the near-continuum flow regime, the Boltzmann-BGK equation is generally sufficient to provide an accurate description of gas dynamics. It reads

$$(2.1) \quad \frac{\partial f}{\partial t} + \boldsymbol{\xi} \cdot \nabla_{\mathbf{x}} f = \nu(f^M - f),$$

where  $f(t, \mathbf{x}, \boldsymbol{\xi})$  is the molecular distribution function with  $t \in \mathbb{R}^+$ ,  $\mathbf{x} \in \Omega \subset \mathbb{R}^D$  ( $D = 1, 2, \text{ or } 3$ ), and  $\boldsymbol{\xi} \in \mathbb{R}^3$  representing time, spatial position, and molecular velocity, respectively. The left-hand side of (2.1) describes the evolution of  $f$  due to the free streaming of molecules, while the right-hand side accounts for molecular collisions via a simplified relaxation process. Besides,  $\nabla_{\mathbf{x}}$  is the gradient operator with respect to  $\mathbf{x}$ , and  $\nu$  denotes the average collision frequency, assumed to be independent of  $\boldsymbol{\xi}$  and inversely proportional to the Knudsen number, i.e.,  $\nu \propto 1/Kn$ . For the BGK collision term,  $f^M$  is the local Maxwellian defined as

$$(2.2) \quad f^M(t, \mathbf{x}, \boldsymbol{\xi}) = \frac{\rho(t, \mathbf{x})}{m_* (2\pi\theta(t, \mathbf{x}))^{3/2}} \exp\left(-\frac{|\boldsymbol{\xi} - \mathbf{u}(t, \mathbf{x})|^2}{2\theta(t, \mathbf{x})}\right),$$

in which  $m_*$  is the mass of a single molecule, and  $\rho$ ,  $\mathbf{u}$ , and  $\theta$  are density, mean velocity, and temperature, respectively. These primary macroscopic quantities are determined by  $f$  through the following relations

$$(2.3) \quad \begin{aligned} \rho(t, \mathbf{x}) &= m_* \int_{\mathbb{R}^3} f(t, \mathbf{x}, \boldsymbol{\xi}) d\boldsymbol{\xi}, \\ \rho(t, \mathbf{x}) \mathbf{u}(t, \mathbf{x}) &= m_* \int_{\mathbb{R}^3} \boldsymbol{\xi} f(t, \mathbf{x}, \boldsymbol{\xi}) d\boldsymbol{\xi}, \\ \rho(t, \mathbf{x}) |\mathbf{u}(t, \mathbf{x})|^2 + 3\rho(t, \mathbf{x})\theta(t, \mathbf{x}) &= m_* \int_{\mathbb{R}^3} |\boldsymbol{\xi}|^2 f(t, \mathbf{x}, \boldsymbol{\xi}) d\boldsymbol{\xi}. \end{aligned}$$

Two additional macroscopic quantities of interest, namely the stress tensor  $\boldsymbol{\sigma}$  and heat flux  $\mathbf{q}$ , are given by

$$(2.4) \quad \begin{aligned} \sigma_{ij}(t, \mathbf{x}) &= m_* \int_{\mathbb{R}^3} (\xi_i - u_i(t, \mathbf{x}))(\xi_j - u_j(t, \mathbf{x})) f(t, \mathbf{x}, \boldsymbol{\xi}) d\boldsymbol{\xi} - \rho(t, \mathbf{x})\theta(t, \mathbf{x})\delta_{ij}, \\ \mathbf{q}(t, \mathbf{x}) &= \frac{m_*}{2} \int_{\mathbb{R}^3} |\boldsymbol{\xi} - \mathbf{u}(t, \mathbf{x})|^2 (\boldsymbol{\xi} - \mathbf{u}(t, \mathbf{x})) f(t, \mathbf{x}, \boldsymbol{\xi}) d\boldsymbol{\xi}, \end{aligned}$$

where  $\delta_{ij}$  is the Kronecker delta symbol, and  $i, j = 1, 2, 3$  represent the Cartesian coordinate directions.

**2.2. Grad's expansion and hyperbolic moment system.** In Grad's moment method, the distribution function  $f$  is expanded into a series in terms of Hermite functions as

$$(2.5) \quad f(t, \mathbf{x}, \boldsymbol{\xi}) = \sum_{\alpha \in \mathbb{N}^3} f_{\alpha}(t, \mathbf{x}) \mathcal{H}_{\alpha}^{[\mathbf{u}, \theta]}(\boldsymbol{\xi}),$$

where  $f_{\alpha}(t, \mathbf{x})$  are the expansion coefficients representing  $\alpha$ th-order moments of  $f$ , and  $\mathcal{H}_{\alpha}^{[\cdot, \cdot]}(\cdot)$  are the corresponding basis functions defined as

$$\mathcal{H}_{\alpha}^{[\mathbf{u}, \theta]}(\boldsymbol{\xi}) = \frac{1}{m_* (2\pi\theta)^{3/2} \theta^{|\alpha|/2}} \prod_{d=1}^3 He_{\alpha_d}(v_d) \exp\left(-\frac{v_d^2}{2}\right), \quad \mathbf{v} = \frac{\boldsymbol{\xi} - \mathbf{u}}{\sqrt{\theta}}, \quad \forall \boldsymbol{\xi} \in \mathbb{R}^3,$$

in which  $|\alpha| = \alpha_1 + \alpha_2 + \alpha_3$  is the sum of all components of the three-dimensional multi-index  $\alpha = (\alpha_1, \alpha_2, \alpha_3) \in \mathbb{N}^3$ , and  $He_n(\cdot)$  is the Hermite polynomial of degree  $n$ , namely,

$$He_n(x) = (-1)^n \exp\left(\frac{x^2}{2}\right) \frac{d^n}{dx^n} \exp\left(-\frac{x^2}{2}\right).$$

Using the orthogonality of Hermite polynomials, we can easily deduce that all basis functions  $\mathcal{H}_{\alpha}^{[\mathbf{u}, \theta]}(\boldsymbol{\xi})$  are orthogonal to each other over  $\mathbb{R}^3$  with respect to the weight function  $\exp(|\mathbf{v}|^2/2)$ , and the expansion coefficients are given by

$$f_{\alpha}(t, \mathbf{x}) = \frac{m_*^2 (2\pi\theta)^{3/2} \theta^{|\alpha|}}{\alpha_1! \alpha_2! \alpha_3!} \int f(t, \mathbf{x}, \boldsymbol{\xi}) \mathcal{H}_{\alpha}^{[\mathbf{u}, \theta]}(\boldsymbol{\xi}) \exp\left(\frac{|\mathbf{v}|^2}{2}\right) d\boldsymbol{\xi}.$$

Then, from relations (2.3) and (2.4) between macroscopic quantities and the distribution function, we have

$$(2.6) \quad \begin{aligned} f_0 &= \rho, \quad f_{e_1} = f_{e_2} = f_{e_3} = 0, \quad \sum_{d=1}^3 f_{2e_d} = 0, \\ \sigma_{ij} &= (1 + \delta_{ij}) f_{e_i + e_j}, \quad q_i = 2f_{3e_i} + \sum_{d=1}^3 f_{2e_d + e_i}, \quad i, j = 1, 2, 3, \end{aligned}$$

where  $e_1$ ,  $e_2$ , and  $e_3$  correspond to the three-dimensional multi-indices  $(1, 0, 0)$ ,  $(0, 1, 0)$ , and  $(0, 0, 1)$ , respectively. It follows that the leading term in the expansion (2.5) exactly recovers the local Maxwellian, that is,  $f^M = f_0 \mathcal{H}_0^{[u, \theta]}(\xi)$ , which implies that Grad's expansion provides an efficient representation of the distribution function for flows close to thermodynamic equilibrium. However, in practice, it is often convenient to expand  $f$  in terms of Hermite functions with generalized parameters  $\varpi$  and  $\vartheta$ , respectively, in place of the local mean velocity  $\mathbf{u}$  and temperature  $\theta$  used in Grad's expansion. In this case, relations similar to (2.6) can be derived accordingly, indicating that all the aforementioned macroscopic quantities of interest can be determined by  $\varpi$ ,  $\vartheta$ , and the low-order coefficients  $f_\alpha$  with  $|\alpha| \leq 3$ . We refer to [18] for the detailed expressions and omit them here for brevity.

Applying the systematic approach of the hyperbolic moment model reduction proposed in [8, 9] to the Boltzmann-BGK equation (2.1), together with Grad's expansion (2.5) and a selected truncation order  $M$ , we obtain a system of equations for  $\mathbf{u}$ ,  $\theta$ , and  $f_\alpha$  with  $|\alpha| \leq M$ , which is referred to as the moment system of order  $M$ , and can be rewritten into a quasi-linear form as

$$(2.7) \quad \frac{\partial \boldsymbol{\varrho}}{\partial t} + \sum_{j=1}^D \mathbf{A}_j(\boldsymbol{\varrho}) \frac{\partial \boldsymbol{\varrho}}{\partial x_j} = \mathcal{Q}(\boldsymbol{\varrho}),$$

by introducing  $\boldsymbol{\varrho}$  as a vector that collects all unknown variables. For conciseness and without loss of clarity, its component-wise expression is not shown explicitly in this work. Nevertheless, several important properties of this moment system are worth mentioning. First, it is globally hyperbolic with all eigenvalues given by  $\mathbf{u} \cdot \mathbf{n} + c_{ij} \sqrt{\theta}$  for any matrix of the form  $n_1 \mathbf{A}_1(\boldsymbol{\varrho}) + \dots + n_D \mathbf{A}_D(\boldsymbol{\varrho})$ , where  $\mathbf{n} = (n_1, \dots, n_D)^T$  is a unit vector, and  $c_{ij}$  denotes the  $i$ th root of the Hermite polynomial  $He_j(x)$ , with  $j = 1, 2, \dots, M+1$ , and  $i = 1, 2, \dots, j$ . Second, its solution shall provide an  $M$ th-order approximation of the distribution function, i.e.,

$$(2.8) \quad f(t, \mathbf{x}, \xi) \approx \sum_{|\alpha| \leq M} f_\alpha(t, \mathbf{x}) \mathcal{H}_\alpha^{[u, \theta]}(\xi),$$

which indicates that the moment system can be interpreted as a semi-discretization of the Boltzmann-BGK equation in velocity space. This allows us to construct unified numerical solvers for the moment system of arbitrary order directly based on the underlying Boltzmann-BGK equation.

Moreover, the moment system is often regarded as an extended hydrodynamic model when  $M \geq 2$ , since its lower-order components include the hydrodynamic equations. In particular, the first component, corresponding to the index  $\alpha = 0$ , turns out to be exactly the continuity equation

$$(2.9) \quad \frac{\partial \rho}{\partial t} + \nabla_{\mathbf{x}} \cdot (\rho \mathbf{u}) = 0.$$

The next three equations, with the indices  $\alpha = e_i$ ,  $i = 1, 2, 3$ , correspond to the momentum equations

$$(2.10) \quad \frac{\partial(\rho \mathbf{u})}{\partial t} + \nabla_{\mathbf{x}} \cdot (\rho \mathbf{u} \otimes \mathbf{u} + p \mathbf{I} + \boldsymbol{\sigma}) = 0,$$

where  $p = \rho \theta$  is the pressure, and  $\mathbf{I}$  is the identity matrix. Finally, by summing the equations for  $\alpha = 2e_i$ ,  $i = 1, 2, 3$ , we can recover the energy equation

$$(2.11) \quad \frac{\partial(\rho E)}{\partial t} + \nabla_{\mathbf{x}} \cdot (\rho E \mathbf{u} + p \mathbf{u} + \mathbf{u} \cdot \boldsymbol{\sigma} + \mathbf{q}) = 0,$$

in which  $E = \frac{1}{2} (3\theta + |\mathbf{u}|^2)$  represents the total energy.

**2.3. Spatial discretization and time integration scheme.** Let  $\Omega$  be a rectangular domain in  $\mathbb{R}^D$ , partitioned by a uniform Cartesian grid with  $N_1 \times \dots \times N_D$  cells. Suppose the grid cell and its center are denoted by  $\mathcal{T}_{\mathbf{i}} = [x_{i_1-1/2}, x_{i_1+1/2}] \times \dots \times [x_{i_D-1/2}, x_{i_D+1/2}]$  and  $\mathbf{x}_{\mathbf{i}} = (x_{i_1}, \dots, x_{i_D})$ , respectively, where  $\mathbf{i} = (i_1, i_2, \dots, i_D)$  is the multi-index with  $i_d = 1, 2, \dots, N_d$  and  $d = 1, \dots, D$ . To derive a unified spatial discretization for the moment system (2.7) of arbitrary order, we return to the Boltzmann-BGK equation (2.1), and integrate it over the  $\mathbf{i}$ th grid cell  $\mathcal{T}_{\mathbf{i}}$ . Then, introducing  $f_{\mathbf{i}}(t, \xi)$  and  $\bar{F}(f_{\mathbf{i}}, f_{\mathbf{i}+e_d})$ , respectively, to represent the cell-averaged distribution function over  $\mathcal{T}_{\mathbf{i}}$  and the numerical flux across the interface between

$\mathcal{T}_i$  and its neighboring cell  $\mathcal{T}_{i+e_d}$ , we obtain a finite volume discretization of the Boltzmann-BGK equation, formally written as

$$(2.12) \quad \frac{df_i}{dt} = - \sum_{d=1}^D \frac{1}{\Delta x_d} [\bar{F}(f_i, f_{i+e_d}) - \bar{F}(f_{i-e_d}, f_i)] + Q(f_i) =: \mathcal{R}_i(\mathbf{f}),$$

where  $\Delta x_d = x_{i_d+1/2} - x_{i_d-1/2}$  is the grid size in the  $d$ th direction,  $Q(f_i)$  describes the collision term, and  $\mathcal{R}_i(\mathbf{f})$  denotes the local residual associated with  $\mathcal{T}_i$ , in which  $\mathbf{f}$  is the collection of all  $f_i$ .

To proceed, let Grad's expansion of order  $M$  be employed for all cell-averaged distribution function, i.e.,

$$(2.13) \quad f_i(t, \boldsymbol{\xi}) \approx \sum_{|\alpha| \leq M} f_{i,\alpha}(t) \mathcal{H}_\alpha^{[u_i, \theta_i]}(\boldsymbol{\xi}).$$

With such an expansion, the BGK collision term directly yields

$$(2.14) \quad Q(f_i) \approx - \sum_{2 \leq |\alpha| \leq M} \nu_i f_{i,\alpha}(t) \mathcal{H}_\alpha^{[u_i, \theta_i]}(\boldsymbol{\xi}).$$

It is also straightforward to show that numerical fluxes, through a suitable projection procedure, can be similarly expressed in terms of the same basis functions, e.g.,

$$(2.15) \quad \bar{F}(f_i, f_{i+e_d}) \approx \sum_{|\alpha| \leq M} \bar{F}_\alpha(f_i, f_{i+e_d}) \mathcal{H}_\alpha^{[u_i, \theta_i]}(\boldsymbol{\xi}).$$

Consequently, substituting these expansions into (2.12), and matching the coefficients for each basis function, we get a nonlinear system with respect to  $u_i$ ,  $\theta_i$ , and  $f_{i,\alpha}$  for  $|\alpha| \leq M$  and  $i$  ranging over all grid cells in  $\Omega$ . Provided that numerical fluxes are constructed consistently with the hyperbolic moment model reduction, this nonlinear system shall constitute a unified spatial discretization for the moment system (2.7).

In the current work, the numerical flux introduced in [12] is adopted. It is essentially a modified HLL flux, with a regularization term accounting for the hyperbolicity of the system. More precisely, we have

$$(2.16) \quad \bar{F}(f_i, f_{i+e_d}) = \hat{F}_{i+\frac{1}{2}e_d} + \tilde{F}_{i+\frac{1}{2}e_d}^-, \quad \bar{F}(f_{i-e_d}, f_i) = \hat{F}_{i-\frac{1}{2}e_d} + \tilde{F}_{i-\frac{1}{2}e_d}^+,$$

where  $\hat{F}_{i+\frac{1}{2}e_d}$  is the HLL flux defined as

$$(2.17) \quad \hat{F}_{i+\frac{1}{2}e_d} = \begin{cases} \xi_d f_i(t, \boldsymbol{\xi}), & \lambda_d^L \geq 0, \\ \frac{\lambda_d^R \xi_d f_i(t, \boldsymbol{\xi}) - \lambda_d^L \xi_d f_{i+e_d}(t, \boldsymbol{\xi}) + \lambda_d^R \lambda_d^L (f_{i+e_d}(t, \boldsymbol{\xi}) - f_i(t, \boldsymbol{\xi}))}{\lambda_d^R - \lambda_d^L}, & \lambda_d^L < 0 < \lambda_d^R, \\ \xi_d f_{i+e_d}(t, \boldsymbol{\xi}), & \lambda_d^R \leq 0, \end{cases}$$

and  $\tilde{F}_{i\pm\frac{1}{2}e_d}^\pm$  denote the regularization terms whose expressions are omitted for simplicity. Here,  $\lambda_d^L$  and  $\lambda_d^R$  are, respectively, the minimal and maximal eigenvalues of  $\mathbf{A}_d(\boldsymbol{q})$ , estimated from the states of both the  $i$ th and  $(i+e_d)$ th cells as

$$(2.18) \quad \lambda_d^L = \min_{j \in \{i, i+e_d\}} \left\{ u_{j,d} - c_M \sqrt{\theta_j} \right\}, \quad \lambda_d^R = \max_{j \in \{i, i+e_d\}} \left\{ u_{j,d} + c_M \sqrt{\theta_j} \right\},$$

in which  $c_M$  is the largest root of the Hermite polynomial  $He_{M+1}(x)$ .

Obviously, appropriate boundary conditions on the domain boundary  $\partial\Omega$  are required to complete the spatial discretization. In most of the experiments presented in section 5, we consider the Maxwell boundary condition, whose detailed treatment within the framework of Grad's expansion can be found in [11, 12]. An exception is the shock structure problem, where a Maxwellian with prescribed boundary density, mean velocity, and temperature would be directly imposed.

Now we turn to the time integration for the system of semi-discretization (2.12). We shall first consider the forward Euler scheme, one of the simplest time-integration schemes, taking the form

$$(2.19) \quad f_i^{n+1} = f_i^n + \Delta t \mathcal{R}_i(\mathbf{f}^n),$$

where the superscript  $n$  is used to label the approximation of variables at time  $t^n$ , with the time step size given by  $\Delta t = t^{n+1} - t^n$ . Due to stability constraints, the time step size is selected according to the CFL condition, that is,

$$(2.20) \quad \Delta t = \min_i \Delta t_i,$$

where the local time step size  $\Delta t_i$  should satisfy

$$(2.21) \quad \Delta t_i \sum_{d=1}^D \frac{|u_{i,d}^n| + c_M \sqrt{\theta_i^n}}{\Delta x_d} = \text{CFL} < 1,$$

with CFL being a user-specified constant.

We conclude this section by noting that, using Grad's expansion for each distribution function, the left- and right-hand sides of (2.19) are expressed in terms of basis functions with possibly different local parameters. As a result, the scheme (2.19) numerically involves two steps, as explained in [21].

**3. Fast iterative moment method.** In this paper, we are primarily concerned with the steady-state solution to the high-order moment system, or equivalently, the Boltzmann-BGK equation, in the regime with small  $Kn$ , as  $t \rightarrow \infty$ . Dropping the time derivatives in (2.12), we arrive at the discrete steady-state problem

$$(3.1) \quad \mathcal{R}_i(\mathbf{f}) = 0,$$

for all  $i$ . At this stage, the forward Euler scheme (2.19) serves as a basic iteration, also known as the Richardson iteration. However, once the moment system is of order  $M \geq 2$ , such that  $Kn$  appears in the higher-order equations via the collision frequency  $\nu$ , the convergence of time-integration-based methods, including the forward Euler scheme, becomes extremely slow as  $Kn$  decreases toward the continuum limit. To address such poor convergence, we shall introduce a novel alternating iteration, referred to as the fast iterative moment (FIM) method, in this section.

**3.1. Alternating iteration framework.** It is well known that the fluid dynamic limit of the Boltzmann equation leads to the hydrodynamic Euler or NSF equations as  $Kn$  tends to zero. When  $Kn < 0.001$ , gas flows fall into the continuum regime, and the classical hydrodynamic equations are typically accurate in describing gas dynamics. It follows that the higher-order moments  $f_\alpha$  with  $|\alpha| \geq 2$  would be negligible, or otherwise well captured by the primary macroscopic quantities  $\rho$ ,  $\mathbf{u}$ , and  $\theta$ . The same holds for the stress tensor  $\boldsymbol{\sigma}$  and heat flux  $\mathbf{q}$ . In contrast, when  $Kn > 0.001$  but remains relatively small, that is, in the near-continuum flow regime, the classical hydrodynamic equations may no longer be adequate, and a high-order moment system involving more equations becomes necessary. Nevertheless, the classical model can still be expected to provide fairly reliable approximations of the primary macroscopic quantities. Moreover, the order  $M$  of the moment system does not need to be very large, and the rest of the higher-order moments  $f_\alpha$ , as well as  $\boldsymbol{\sigma}$  and  $\mathbf{q}$ , are anticipated either to remain small or vary slowly during time integration.

Motivated by the above observations, and noting that the hydrodynamic equations (2.9)–(2.11) can, in some sense, be regarded as a subsystem extracted from the full moment system, it is natural to expect that this subsystem could be solved more efficiently and thereby utilized to accelerate convergence toward the steady-state solution of the full moment system. Building upon this idea, we consequently propose a framework of alternating iteration between the high-order moment system (HMS) and the hydrodynamic equations (HEs), which forms the core of the resulting FIM method. A schematic flowchart of this FIM alternating iteration is illustrated in Figure 1.

Specifically, starting from an initial guess for the solution  $\mathbf{f}$  of the HMS, we first perform a few basic iterations, for example, one or two steps of the forward Euler scheme (2.19), on the HMS to update  $\mathbf{f}$ . The primary macroscopic quantities  $\rho$ ,  $\mathbf{u}$ , and  $\theta$  are then extracted from  $\mathbf{f}$  and updated by solving the HEs, subject to consistent  $\boldsymbol{\sigma}$ ,  $\mathbf{q}$ , and hydrodynamic boundary conditions, all evaluated also from the current  $\mathbf{f}$ . The updated  $\rho$ ,  $\mathbf{u}$ , and  $\theta$  are subsequently fed back into  $\mathbf{f}$ , which continues to be updated by repeatedly solving the HMS and HEs, in turn as described above, until convergence is achieved. In the next subsections, the main ingredients of the hydrodynamic part in the alternating iteration, including a numerical scheme for the HEs and a formulation ensuring discretization consistency with the HMS, will be described in detail, followed by a complete FIM algorithm.

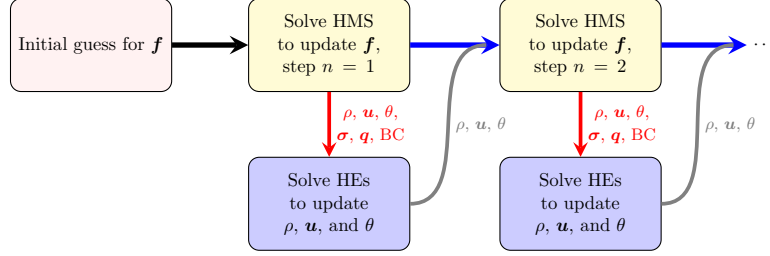


Figure 1: Flowchart of the alternating iteration in the FIM method. HMS: high-order moment system; HEs: hydrodynamic equations; BC: consistent hydrodynamic boundary conditions.

**3.2. Numerical scheme for hydrodynamic equations.** The hydrodynamic equations (2.9)–(2.11) can be rewritten in vector form as

$$(3.2) \quad \frac{\partial U}{\partial t} + \nabla_x \cdot \mathbf{F}(U) = 0,$$

where

$$U = \begin{bmatrix} \rho \\ \rho \mathbf{u} \\ \rho E \end{bmatrix}, \quad \mathbf{F}(U) = \begin{bmatrix} \rho \mathbf{u} \\ \rho \mathbf{u} \otimes \mathbf{u} + p \mathbf{I} + \boldsymbol{\sigma} \\ \rho E \mathbf{u} + p \mathbf{u} + \mathbf{u} \cdot \boldsymbol{\sigma} + \mathbf{q} \end{bmatrix}.$$

Applying the finite volume method to (3.2) over the  $i$ th grid cell  $\mathcal{T}_i$ , we obtain

$$(3.3) \quad \frac{dU_i}{dt} = - \sum_{d=1}^D \frac{1}{\Delta x_d} [\bar{\mathbf{F}}(U_i, U_{i+e_d}) - \bar{\mathbf{F}}(U_{i-e_d}, U_i)] =: \mathcal{R}_i^{\text{hydro}}(U),$$

where  $U_i$  is the cell average of  $U$  associated with  $\mathcal{T}_i$ , and  $\mathcal{R}_i^{\text{hydro}}(U)$  denotes the corresponding local residual of the hydrodynamic equations, with  $\mathbf{U}$  representing the collection of all  $U_i$ . Following the treatment for the moment system, the HLL flux is also employed for the numerical flux  $\bar{\mathbf{F}}(\cdot, \cdot)$ . Thus, we have

$$(3.4) \quad \bar{\mathbf{F}}(U_i, U_{i+e_d}) = \begin{cases} \mathbf{F}(U_i), & \lambda_d^L \geq 0, \\ \frac{\lambda_d^R \mathbf{F}(U_i) - \lambda_d^L \mathbf{F}(U_{i+e_d}) + \lambda_d^R \lambda_d^L (U_{i+e_d} - U_i)}{\lambda_d^R - \lambda_d^L}, & \lambda_d^L < 0 < \lambda_d^R, \\ \mathbf{F}(U_{i+e_d}), & \lambda_d^R \leq 0. \end{cases}$$

Here it is important to emphasize that  $\lambda_d^L$  and  $\lambda_d^R$  must be evaluated using the same expressions as in (2.18), which is essential for ensuring consistency with the spatial discretization (3.1) of the moment system.

The semi-discretization (3.3) can be solved similarly using the forward Euler scheme, which yields

$$(3.5) \quad U_i^{m+1} = U_i^m + \Delta t \mathcal{R}_i^{\text{hydro}}(U^m),$$

where the time step size  $\Delta t$  is determined again by the CFL condition given in (2.20) and (2.21). In each alternating iteration, this scheme might be executed over multiple time steps, beginning with an initial guess  $\mathbf{U}^0$  obtained from the current  $\mathbf{f}$ , until the numerical solution  $\mathbf{U}^m$  has sufficiently evolved or converged.

**3.3. Consistent constitutive and boundary conditions.** In order to guarantee that the hydrodynamic equations (3.2) give rise to steady-state macroscopic quantities  $\rho$ ,  $\mathbf{u}$ , and  $\theta$  exactly matching those obtained from the high-order moment system, it remains necessary to impose consistent constitutive relations and boundary conditions for the hydrodynamic equations. To this end, we adopt the following simplified approaches in the present FIM method.

As in the NSF equations, the stress tensor  $\boldsymbol{\sigma}$  and heat flux  $\mathbf{q}$  that appear in (3.2) can be determined from the primary macroscopic quantities  $\rho$ ,  $\mathbf{u}$ , and  $\theta$ . To avoid additional modeling assumptions, however, they

are instead evaluated from the solution  $\mathbf{f}$  of the moment system and kept unchanged during the integration (3.5) in each alternating iteration.

Similarly, Dirichlet-type hydrodynamic boundary conditions are prescribed, rather than being directly derived from the primary macroscopic quantities. Precisely speaking, the ghost-cell distribution function  $f^g$  outside the domain  $\Omega$  is first constructed from the solution  $\mathbf{f}$  to satisfy the boundary conditions of the moment system. The macroscopic quantities  $\rho^g$ ,  $\mathbf{u}^g$ , and  $\theta^g$ , as well as  $\boldsymbol{\sigma}^g$  and  $\mathbf{q}^g$ , are then evaluated from  $f^g$  and held fixed during the integration (3.5) until the next alternating iteration. With these ghost-cell macroscopic quantities available, all numerical fluxes (3.4) across the domain boundary can be fully determined, thereby completing the specification of the hydrodynamic boundary conditions.

**3.4. Complete FIM algorithm.** Incorporating all the ingredients described above, the framework for one step of the FIM alternating iteration, which advances the solution from a given approximation  $\mathbf{f}^n$  to a new one  $\mathbf{f}^{n+1}$ , is summarized in Algorithm 3.1. Therein,  $Tol$  is a prescribed tolerance indicating the convergence criterion of the hydrodynamic solver, while  $\gamma_1$  and  $\gamma_2$  are user-defined positive integers controlling the number of iterations for the moment and hydrodynamic solvers, respectively. All of them are chosen to balance the computational cost per alternating iteration with the convergence rate.

Performing the algorithm until convergence immediately yields a steady-state solver for the Boltzmann-BGK equation. Throughout the paper, both this solver and the algorithm itself are conveniently referred to as the FIM-1 solver. Notably, the moment and hydrodynamic solvers in the algorithm can, in principle, be replaced by alternatives to obtain further improved FIM solvers. Several such strategies will be discussed in the next section, while this section closes with two remarks on the proposed FIM method.

*Remark 3.1.* In comparison to the NMLM solver proposed in [21, 18], which accelerates convergence by using lower-order model corrections, the FIM solver can be regarded as a two-level NMLM solver, where the hydrodynamic equations (3.2) serve as the lower-order model. However, instead of the restriction and prolongation operators designed under the original NMLM framework, a new alternative strategy for transferring information between the high- and lower-order models is introduced. As demonstrated in section 5, this redesigned two-level NMLM solver, namely, the FIM solver, improves both robustness and efficiency, especially in the near-continuum flow regime.

*Remark 3.2.* The FIM method also shares, to some extent, a similar philosophy and convergence behavior with the GSIS introduced in [25, 32], as both methods find the steady-state solution through alternating iterations between the Boltzmann and hydrodynamic equations. However, unlike the GSIS which is typically developed within the discrete velocity framework, the present FIM method is formulated in the framework of the moment method. Moreover, since the hydrodynamic equations arise as a subsystem of the moment system, the FIM method requires consistent spatial discretizations for both systems to ensure that they yield identical numerical values of the primary macroscopic quantities. This consistency requirement is crucial for guaranteeing the convergence of the overall alternating iteration.

---

**Algorithm 3.1** One step of the FIM alternating iteration  $\mathbf{f}^{n+1} = \text{FIM}(\mathbf{f}^n)$

---

**Input:** Grid,  $\mathbf{f}^n$

**Output:** The new approximation  $\mathbf{f}^{n+1}$

---

- 1: Update  $\mathbf{f}$  from  $\mathbf{f}^n$  by performing  $\gamma_1$  steps of a basic moment solver, e.g., the forward Euler scheme (2.19), denoted as  $\tilde{\mathbf{f}} = \text{MSolver}^{\gamma_1}(\mathbf{f}^n)$ ;
  - 2: Compute  $\tilde{\rho}$ ,  $\tilde{\mathbf{u}}$ ,  $\tilde{\theta}$ ,  $\tilde{\boldsymbol{\sigma}}$ , and  $\tilde{\mathbf{q}}$  on all grid cells, and construct  $f^g$  on all ghost cells from  $\tilde{\mathbf{f}}$ ;
  - 3: Construct the initial guess  $\mathbf{U}^0$  with  $U_i^0 = [\tilde{\rho}_i, \tilde{\rho}_i \tilde{\mathbf{u}}_i, \frac{1}{2} \tilde{\rho}_i (3\tilde{\theta}_i + |\tilde{\mathbf{u}}_i|^2)]^T$  for the hydrodynamic equations;
  - 4: Fix the stress tensor and heat flux in the hydrodynamic equations by  $\tilde{\boldsymbol{\sigma}}$  and  $\tilde{\mathbf{q}}$ , respectively;
  - 5: Compute  $\rho^g$ ,  $\mathbf{u}^g$ ,  $\theta^g$ ,  $\boldsymbol{\sigma}^g$ , and  $\mathbf{q}^g$  on all ghost cells from the corresponding  $f^g$ ;
  - 6: Set  $m = 0$ , and  $diff = 1$ ;
  - 7: **while**  $m < \gamma_2$  and  $diff > Tol$  **do**
  - 8:   Calculate  $\mathbf{U}^{m+1}$  from  $\mathbf{U}^m$  by performing one step of a hydrodynamic solver, e.g., the forward Euler scheme (3.5), denoted as  $\mathbf{U}^{m+1} = \text{HSolver}(\mathbf{U}^m)$ ;
  - 9:   Evaluate  $diff$  as the  $L_1$  norm of the difference between successive solutions:  $diff = \|\mathbf{U}^{m+1} - \mathbf{U}^m\|_1$ ;
  - 10:   Set  $m = m + 1$ ;
  - 11: **end while**
  - 12: Extract  $\rho^m$ ,  $\mathbf{u}^m$ , and  $\theta^m$  from  $\mathbf{U}^m$ ;
  - 13: **return**  $\mathbf{f}^{n+1}$ , constructed from  $\tilde{\mathbf{f}}$  by replacing  $\tilde{\rho}$ ,  $\tilde{\mathbf{u}}$ , and  $\tilde{\theta}$  with  $\rho^m$ ,  $\mathbf{u}^m$ , and  $\theta^m$ , respectively.
-



**4. Further acceleration strategies.** To further enhance the efficiency and robustness of the FIM method, this section is devoted to extending the previous FIM-1 solver by incorporating several acceleration strategies, including a semi-implicit scheme, the Gauss-Seidel method with a cell-by-cell sweeping strategy, and a nonlinear multigrid method. The resulting FIM solvers are summarized at the end of the section.

**4.1. Semi-implicit scheme for moment system.** Due to the presence of  $1/Kn$  in the collision term, the moment system of order  $M \geq 2$  exhibits increasing stiffness as  $Kn \rightarrow 0$ . As a consequence, the forward Euler scheme (2.19), with the time step size determined by (2.20) and (2.21), might become unstable for small  $Kn$ , leading to significantly slower convergence or even divergence of the FIM solver. To overcome this instability, we hereafter consider a simple semi-implicit approach for the moment system, in which the collision term is treated implicitly.

Specifically, replacing the discrete collision term  $Q(f_i^n)$  with  $Q(f_i^{n+1})$  in the forward Euler scheme (2.19) and rearranging terms yields

$$(4.1) \quad f_i^{n+1} - \Delta t Q(f_i^{n+1}) = f_i^n - \Delta t \mathcal{A}_i(f^n),$$

where  $\mathcal{A}_i(f^n)$  represents the remaining part of  $-\mathcal{R}_i(f^n)$ , namely, the contribution from the spatial discretization of the convection term  $\xi \cdot \nabla_x f$ . As described in subsection 2.3, this would give rise to

$$(4.2) \quad f_{i,0}^{n+1} \mathcal{H}_0^{[u_i^{n+1}, \theta_i^{n+1}]}(\xi) + \sum_{2 \leq |\alpha| \leq M} (1 + \Delta t \nu_i^{n+1}) f_{i,\alpha}^{n+1} \mathcal{H}_\alpha^{[u_i^{n+1}, \theta_i^{n+1}]}(\xi) = \sum_{|\alpha| \leq M} g_{i,\alpha} \mathcal{H}_\alpha^{[u_i^n, \theta_i^n]}(\xi),$$

by noting that Grad's expansion of order  $M$  is employed for both  $f_i^n$  and  $f_i^{n+1}$ . Here  $g_{i,\alpha}$  denote the resulting coefficients evaluated from the right-hand side of (4.1). Multiplying both sides of the above equation by  $(1, \xi, |\xi|^2)^T$ , and integrating over the whole velocity space as in (2.3), we can establish generalized relations for the macroscopic quantities and lower-order expansion coefficients, from which we get

$$(4.3) \quad f_{i,0}^{n+1} = g_{i,0}, \quad \mathbf{u}_i^{n+1} = \mathbf{u}_i^n + \frac{1}{g_{i,0}} (g_{i,e_1}, g_{i,e_2}, g_{i,e_3})^T, \quad \theta_i^{n+1} = \theta_i^n + \frac{2}{3} \sum_{d=1}^3 \frac{g_{i,2e_d}}{g_{i,0}} - \frac{|\mathbf{u}_i^{n+1} - \mathbf{u}_i^n|^2}{3}.$$

The right-hand side of (4.2) is then projected onto the same basis functions as those on the left-hand side. With these re-expansion coefficients denoted by  $\tilde{g}_{i,\alpha}$ , we finally obtain

$$(4.4) \quad f_{i,\alpha}^{n+1} = \frac{1}{1 + \Delta t \nu_i^{n+1}} \tilde{g}_{i,\alpha}, \quad \text{for } |\alpha| \geq 2.$$

It can be readily observed that the above semi-implicit scheme (SIS) incurs almost the same computational cost per time step as the forward Euler scheme (2.19). However, it offers considerably improved numerical stability, being particularly effective in mitigating stiffness caused by small  $Kn$ . This stability property is formalized in the following theorem.

**THEOREM 4.1.** *The semi-implicit scheme (SIS) described in (4.3) and (4.4) is stable, provided that the time step size  $\Delta t$  satisfies the CFL condition (2.20) and (2.21).*

*Proof.* First, it is well known that the CFL condition described in (2.20) and (2.21) ensures the numerical stability of the convection procedure, i.e., the computation of the right-hand side in (4.1), indicating that the amplification factor of this step is no greater than 1. To be specific, given a small perturbation  $\delta f_i^n$  of the  $n$ th approximation  $f_i^n$ , the perturbation  $\delta g_i$  resulting from evaluating the right-hand side of (4.2) satisfies

$$\|\delta g\| \leq C_1 \|\delta f^n\|,$$

for some constant  $C_1 \leq 1$ , where  $\delta g$  and  $\delta f^n$  are the collection of all  $\delta g_i$  and  $\delta f_i^n$ , respectively.

Second, the projection procedure, which re-expands the right-hand side of (4.2) onto the basis functions associated with the updated parameters  $\mathbf{u}_i^{n+1}$  and  $\theta_i^{n+1}$ , can be carried out analytically, as demonstrated in [17]. It follows that the computation of (4.3) and the re-expansion coefficients  $\tilde{g}_{i,\alpha}$  is numerically stable. Thus, the corresponding perturbation  $\delta \tilde{g}_i$  fulfills

$$\|\delta \tilde{g}_i\| \leq C_2 \|\delta g_i\|,$$

for some constant  $C_2 \leq 1$ .

In the last computational step (4.4), it is easy to show that each coefficient  $f_{i,\alpha}^{n+1}$  with  $|\alpha| \geq 2$  is scaled by a factor strictly less than 1, since  $\Delta t \nu_i^{n+1} > 0$ . Hence, the final perturbation  $\delta f_i^{n+1}$  satisfies

$$\|\delta f_i^{n+1}\| < \|\delta \tilde{g}_i\|.$$

Combining all the above inequalities, we then obtain

$$\|\delta \mathbf{f}^{n+1}\| < \|\delta \tilde{\mathbf{g}}\| \leq C_2 \|\delta \mathbf{g}\| \leq C_3 \|\delta \mathbf{f}^n\|,$$

for some constant  $C_3 \leq 1$ , where  $\delta \mathbf{f}^{n+1}$  and  $\delta \tilde{\mathbf{g}}$  denote the collection of all  $\delta f_i^{n+1}$  and  $\delta \tilde{g}_i$ , respectively. Therefore, the proposed SIS scheme is stable under the given CFL condition, with an overall amplification factor bounded by 1.  $\square$

**4.2. Gauss-Seidel method with cell-by-cell sweeping.** As revealed in [21, 18, 19], the convergence can be effectively improved by modifying the forward Euler scheme (2.19), which is essentially a Jacobi-type iteration, into a Gauss-Seidel iteration with a cell-by-cell sweeping strategy. In this Gauss-Seidel method, the solution is updated cell by cell along some prescribed sweeping directions, with the latest approximation on each cell directly utilized in computations for subsequent cells. Apparently, such an approach can be extended to all previously introduced moment and hydrodynamic solvers within the FIM method.

In particular, for the moment system, incorporating the Gauss-Seidel method into (4.1), we can modify the SIS into the following scheme

$$(4.5) \quad f_i^{n+1} - \Delta t_i \mathcal{Q}(f_i^{n+1}) = f_i^n - \Delta t_i \mathcal{A}_i(\mathbf{f}^*),$$

where the local time step size  $\Delta t_i$  in place of the global one is employed, and  $\mathbf{f}^*$  is initially set to  $\mathbf{f}^n$ . During the sweeping process, the  $i$ th component of  $\mathbf{f}^*$  is updated to the new approximation  $f_i^{n+1}$  immediately once it becomes available.

Similarly, for the hydrodynamic equations (3.2), applying the Gauss-Seidel method to the forward Euler scheme (3.5) leads to

$$(4.6) \quad \mathbf{U}_i^{m+1} = \mathbf{U}_i^m + \Delta t_i \mathcal{R}_i^{\text{hydro}}(\mathbf{U}^*),$$

where  $\mathbf{U}^*$  is defined analogously to  $\mathbf{f}^*$ . That is,  $\mathbf{U}^*$  is initialized by  $\mathbf{U}^m$ , and updated cell by cell as the new approximation  $\mathbf{U}_i^{m+1}$  becomes available during the sweep.

It remains to specify the sweeping directions, which play a crucial role in the performance of the above Gauss-Seidel schemes. In this work, we adopt a symmetric sweeping strategy for both schemes (4.5) and (4.6), as its effectiveness and robustness have been verified in [21, 18] by the resulting symmetric Gauss-Seidel (SGS) iteration modified from the forward Euler scheme (2.19). Specifically, in the one-dimensional case, the sweeping strategy for a single SGS iteration consists of a forward sweep followed by a backward sweep over all grid cells. In the two-dimensional case, it involves two opposite sweeping directions, as illustrated in Figure 2, where the spatial coordinates  $x_1$  and  $x_2$  are replaced by  $x$  and  $y$ , respectively, with the convention used throughout. In conjunction with this symmetric sweeping strategy, the Gauss-Seidel iteration defined in (4.5) will henceforth be abbreviated as the SISGS iteration for convenience.

**4.3. Nonlinear multigrid method.** The nonlinear multigrid (NMG) method, also known as the full approximation scheme (FAS), is another well-established acceleration technique for solving nonlinear problems [5, 26]. It provides a general framework, that readily extends a single level solver into a multi-level one, where the single level solver is utilized as the smoother, and coarse level corrections are introduced to accelerate the convergence of the solution on the finest level. Following this framework with appropriate restriction and prolongation operators, we have previously developed two types of nonlinear multi-level solvers for the discrete steady-state problem (3.1): an NMG iteration based on spatial coarse grid corrections [20, 19], where all grid levels adopt the same order of the moment system, and an NMLM iteration based on lower-order model corrections [21, 18], where all model levels share the same spatial grid. Both the NMG and NMLM iterations have shown to significantly improve computational efficiency.

Motivated by this, it is natural to construct new NMG solvers by employing one of the FIM solvers as the smoother on all grid levels. To this end, we first clarify that the coarse grid problem associated with the

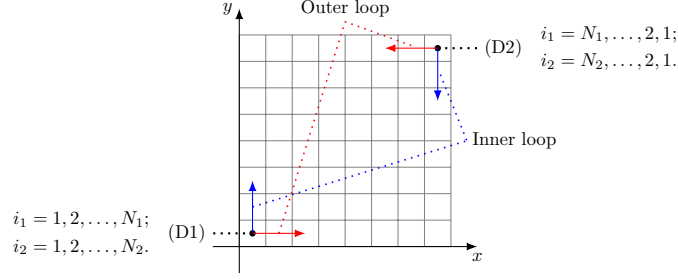


Figure 2: The sketch of sweeping directions (D1) and (D2) in two-dimensional case.

Table 1: FIM solver setup.

FIM solver	Schemes	
	High-order moment system	Hydrodynamic equations
FIM-1	Forward Euler (2.19)	Forward Euler (3.5)
FIM-2	SIS (4.3) and (4.4)	Forward Euler (3.5)
FIM-3	SISGS (4.5)	SGS (4.6)

finest level problem (3.1) is defined in the form

$$(4.7) \quad \mathcal{R}_i(\mathbf{f}) = r_i(\boldsymbol{\xi}),$$

where the right-hand side  $r_i(\boldsymbol{\xi})$  is precomputed and independent of the unknown solution  $\mathbf{f}$ , in accordance with the standard NMG framework. Accordingly, the corresponding hydrodynamic equations on the same grid level take the form

$$(4.8) \quad \mathcal{R}_i^{\text{hydro}}(\mathbf{U}) = r_i^{\text{hydro}}.$$

For the purpose of consistency, the right-hand side  $r_i^{\text{hydro}}$  should not be computed in the same manner as the computation of  $r_i(\boldsymbol{\xi})$ , but instead evaluated from  $r_i(\boldsymbol{\xi})$  via the same procedure as that used to derive the left-hand side. With the coarse grid problem and the associated hydrodynamic equations defined as above, the FIM alternating iteration can be conveniently applied with only minimal adjustments, compared to its application described in previous subsections for the original problem (3.1). Incorporating the remaining components of the NMG method introduced in [20, 19], a new NMG solver can thus be obtained.

*Remark 4.2.* It is noteworthy that, in some sense, the NMLM solver can be viewed as a multigrid method in velocity space [18], and the FIM solver can be interpreted as a two-level NMLM solver. Consequently, the NMG solver that employs the FIM solver as the smoother constitutes an integrated multi-level method, which accelerates convergence by simultaneously accounting for coarse level corrections in both spatial and velocity spaces. However, it is also observed that replacing the smoother with the original two-level NMLM solver does not result in a solver as robust as the present integrated multi-level method.

**4.4. FIM solver family.** With the acceleration strategies introduced above, the FIM method gives rise to a family of solvers, which share a common alternating iteration framework, but differ in the specific numerical schemes used for the moment system and the hydrodynamic equations. In addition to the FIM-1 solver, other FIM solvers investigated in our numerical experiments include the FIM-2 and FIM-3 variants. The corresponding schemes adopted in these FIM solvers are summarized in Table 1.

Moreover, several further enhanced solvers can be constructed within the NMG framework by employing one of the FIM solvers as the smoother. For brevity, the resulting FIM-based NMG solver is referred to as the NMG solver in the following numerical experiments, as only the version using the FIM-3 solver as the smoother is taken into account.

**5. Numerical experiments.** To illustrate the performance of the proposed solvers, we carry out three numerical experiments, including the planar Couette flow, the shock structure, and the lid-driven cavity flow. In all experiments, the test gas is argon, with a molecular mass of  $m_* = 6.63 \times 10^{-26}$  kg. Unless otherwise specified, the following settings are adopted. The CFL number controlling the time step size, the tolerance for convergence, and the number of steps for the moment solver in each FIM alternating iteration, are set to  $\text{CFL} = 0.8$ ,  $\text{Tol} = 10^{-8}$ , and  $\gamma_1 = 1$ , respectively. For the associated NMG solver, a V-cycle is employed with pre-, post- and coarsest-smoothing steps chosen as  $s_1 = s_2 = 2$ , and  $s_3 = 4$ , respectively, to achieve a good balance between convergence rate and computational efficiency. Moreover, the total number of grid levels in the NMG solver is selected such that the coarsest grid consists of 8 cells in the one-dimensional case and  $8 \times 8$  cells in the two-dimensional case, as adopted in [20, 19].

Additionally, in order to ensure consistency with the steady-state solution obtained by time-integration methods, the correction mentioned in [20, 19] is also applied at each FIM alternating iteration or NMG iteration, except in the shock structure experiment, where the prescribed boundary conditions are sufficient to guarantee a unique steady-state solution.

**5.1. Planar Couette flow.** The first example is the planar Couette flow, which is a widely used one-dimensional benchmark problem [20, 33, 32]. For convenience, we consider the same dimensionless setup and parameters as those used in [12, 20]. Particularly, the gas is confined between two infinite parallel plates separated by a distance  $L = 1$ . Both plates are maintained at the temperature of  $\theta^W = 1$ , and move in opposite directions along the plate with a relative velocity  $\mathbf{u}^W = (0, 1.2577, 0)^T$ . The collision frequency  $\nu$  is defined as

$$(5.1) \quad \nu = \sqrt{\frac{\pi}{2}} \frac{1}{Kn} \rho \theta^{1-\omega},$$

where  $\omega = 0.81$  is the viscosity index. In all tests, the gas is initially assumed to be uniformly distributed by the global Maxwellian with the macroscopic quantities specified as

$$(5.2) \quad \rho_0 = 1, \quad \mathbf{u}_0 = 0, \quad \theta_0 = 1.$$

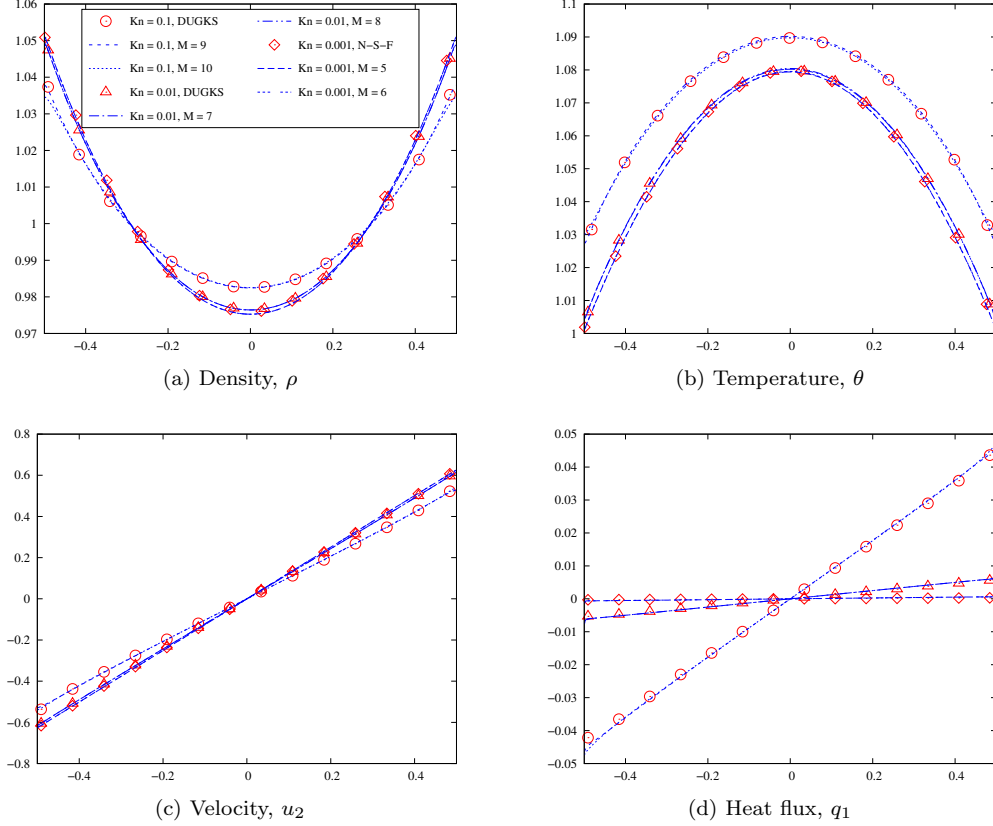
Driven by the motion of the plates, it then gradually evolves toward a steady state.

**5.1.1. Solution validation.** Three different Knudsen numbers in the near-continuum flow regime, namely  $Kn = 0.1, 0.01$ , and  $0.001$ , are investigated. For comparison and validation, reference solutions are obtained from the dugksFoam solver introduced in [31] for  $Kn = 0.1$  and  $0.01$ , and from the NSF equations for  $Kn = 0.001$ . As mentioned in previous sections and observed in [12, 20], the order  $M$  of up to 9 or 10 may be required for the moment system to generate satisfactory results at  $Kn = 0.1$ , while a smaller value of  $M$  would be sufficient for a smaller  $Kn$ . Accordingly, we just take  $M = 9, 10$  for  $Kn = 0.1$ ,  $M = 7, 8$  for  $Kn = 0.01$ , and  $M = 5, 6$  for  $Kn = 0.001$ , respectively, for simplicity. Numerical solutions for the density  $\rho$ , temperature  $\theta$ , vertical velocity  $u_2$ , and heat flux  $q_1$  on the grid with  $N_1 = 1024$  are presented in Figure 3. It can be seen that all of our results agree well with the corresponding references, which confirm the validity of the high-order moment system.

**5.1.2. Performance of basic moment solvers.** The robustness and convergence behavior of the SIS and SISGS iterations, as well as the forward Euler scheme (2.19), are first examined, by performing them directly as basic moment solvers. The total number of iterations and the corresponding wall-clock time, taken by these solvers to reach the steady state on the grid with  $N_1 = 512$ , are listed in Table 2.

As expected and consistent with algorithmic characteristics, the convergence of all three methods deteriorates significantly as  $Kn$  decreases toward the continuum flow regime, leading to a substantial increase in the total number of iterations. Even worse, the forward Euler scheme fails to converge at  $Kn = 0.001$ . Although reducing the CFL number could eventually enable the forward Euler scheme to converge, the SIS remains stable and convergent with the default  $\text{CFL} = 0.8$ . This clearly shows the superior robustness of the SIS over the forward Euler scheme at small  $Kn$ . In contrast, for  $Kn = 0.1$  and  $0.01$  where both the forward Euler scheme and SIS converge, these two methods require approximately the same number of iterations and wall-clock time, indicating comparable performance in such cases.

Moreover, benefiting from the symmetric cell-by-cell sweeping strategy, the SISGS iteration greatly accelerates convergence. Specifically, it reduces the total number of iterations to less than one-third and

Figure 3: Numerical solutions of Couette flow at different  $Kn$  on the uniform grid with  $N_1 = 1024$ .Table 2: Performance of basic moment solvers for Couette flow with  $N_1 = 512$ . Euler: forward Euler scheme; SIS: semi-implicit scheme; SISGS: SIS-based symmetric Gauss-Seidel iteration; “—”: failed to converge.

$Kn$	$M$	Iterations			Wall-clock time (s)		
		Euler	SIS	SISGS	Euler	SIS	SISGS
0.1	10	62074	62068	18042	13469.29	13580.11	5965.08
	9	58413	58407	16912	9987.99	10078.74	4282.54
0.01	8	217947	217941	62472	27109.30	27178.26	11834.03
	7	205063	205057	58336	18229.03	18594.80	7918.06
0.001	6	—	450617	128418	—	28260.00	12192.43
	5	—	435694	122754	—	18604.39	7826.48

the wall-clock time by more than half, compared to the SIS in all tests. Consequently, the SISGS iteration achieves a considerable improvement in efficiency over both the forward Euler scheme and SIS. However, all three methods exhibit similar scaling behavior with respect to the grid number  $N_1$ . As shown in Table 3, when  $N_1$  is doubled, the total number of iterations for  $Kn = 0.1$  roughly doubles, accompanied by a nearly fourfold increase in wall-clock time. Meanwhile, this scaling behavior also deteriorates as  $Kn$  decreases, resulting in the total number of iterations growing by a factor exceeding 3 for both SIS and SISGS methods at  $Kn = 0.001$ .

Additionally, despite the notable increase in the number of iterations as  $Kn$  decreases, the overall growth in wall-clock time, as shown in Table 2, remains relatively moderate. This is mainly because lower orders of the moment system are utilized for smaller  $Kn$ , thereby reducing the computational cost per iteration.

Table 3: Iterations of basic moment solvers for Couette flow on grids with  $N_1 = 128$  and 256. The Ratio columns show the associated ratios between successive grids, with data for  $N_1 = 512$  taken from Table 2.

	$N_1$	$Kn = 0.1, M = 9$		$Kn = 0.01, M = 7$		$Kn = 0.001, M = 5$	
		Iterations	Ratio	Iterations	Ratio	Iterations	Ratio
Euler	128	12679	2.19	28150	2.83		
	256	27718	2.11	79526	2.58		
SIS	128	12675	2.19	28147	2.83	36847	3.49
	256	27713	2.11	79521	2.58	128748	3.38
SISGS	128	3706	2.17	8061	2.81	10619	3.45
	256	8043	2.10	22671	2.57	36668	3.35

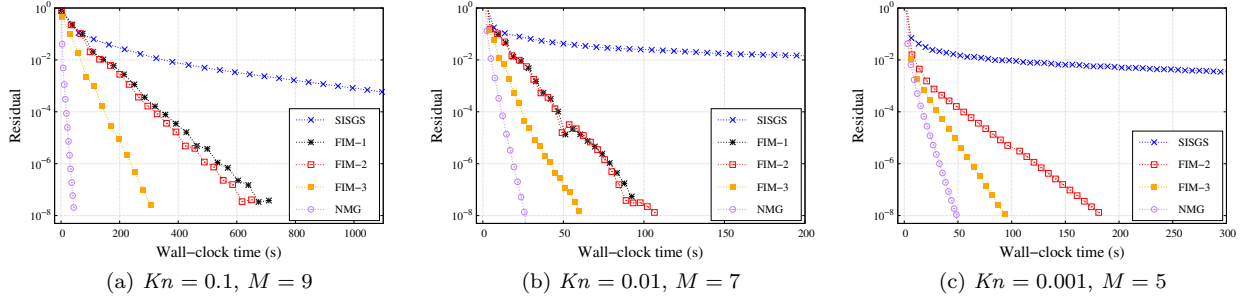
Table 4: Performance of FIM solvers for Couette flow with  $N_1 = 512$  and  $\gamma_2 = 40, 300, 600$  for  $Kn = 0.1, 0.01, 0.001$ , respectively.  $T_r$ : wall-clock time ratio of FIM-3 to SISGS; “-”: unavailable.

$Kn$	$M$	Iterations			Wall-clock time (s)			$T_r$
		FIM-1	FIM-2	FIM-3	FIM-1	FIM-2	FIM-3	
0.1	10	4454	4463	1247	1023.89	924.81	441.86	7.4 %
	9	4166	4176	1167	737.20	677.05	321.27	7.5 %
0.01	8	557	660	203	123.12	142.42	74.33	0.63 %
	7	525	613	194	96.82	108.63	60.38	0.76 %
0.001	6	-	824	249	-	205.74	104.24	0.85 %
	5	-	799	242	-	185.03	93.79	1.2 %

**5.1.3. Performance of FIM and NMG solvers.** Now let us turn to investigating the performance of the FIM solvers. As stated in section 3, when  $Kn$  is small, the hydrodynamic equations are able to predict the primary macroscopic quantities  $\rho$ ,  $\mathbf{u}$ , and  $\theta$  reasonably well, while the remaining moments, including  $\boldsymbol{\sigma}$  and  $\mathbf{q}$ , tend to evolve more slowly. Supported by this observation and several preliminary simulations, we set the parameter  $\gamma_2$  in each FIM alternating iteration to 40, 300, and 600 for  $Kn = 0.1, 0.01$ , and 0.001, respectively. This allows the primary macroscopic quantities to evolve sufficiently before updating the other moments, which in turn improves computational efficiency by accelerating convergence.

The total number of iterations and the associated wall-clock time for the FIM-1, FIM-2, and FIM-3 solvers on the grid with  $N_1 = 512$  are presented in Table 4. Compared to the results of the corresponding basic moment solver shown in Table 2, the three FIM solvers drastically reduce the number of iterations across all cases, indicating a remarkable improvement in convergence rate, especially when  $Kn$  is small. In more detail, at  $Kn = 0.1$ , the total number of iterations for each FIM solver drops by exceeding one order of magnitude, requiring only a few thousand iterations to achieve the steady state. As  $Kn$  decreases to 0.01 and 0.001, the total number of iterations does not increase significantly, unlike what is observed for the basic moment solvers. Instead, it continues to decline, falling to less than 1/5 of the number at  $Kn = 0.1$ . For instance, the FIM-3 solver converges within no more than 250 iterations. Consequently, the computational cost is dramatically reduced, as reflected in the last column of Table 4, which lists the wall-clock time ratio of the FIM-3 solver to the basic SISGS solver. More specifically, when  $Kn = 0.1$ , the FIM-1, FIM-2, and FIM-3 solvers require less than 8% of the wall-clock time relative to their corresponding basic moment solvers, namely, the forward Euler scheme, the SIS, and the SISGS iteration, respectively. By contrast, these wall-clock time ratios drop further to below 0.8% at  $Kn = 0.01$ , and then rebound slightly to reach up to 1.2% at  $Kn = 0.001$ . This rebound should be mainly attributed to the use of a moderately large value of  $\gamma_2$ , which has not yet been carefully optimized, leading to both a higher per-iteration cost and a limited increase in the number of iterations, in comparison with the case at  $Kn = 0.01$ .

To explore the behavior of the FIM solvers throughout the iteration process, we illustrate their convergence histories in terms of wall-clock time, alongside those of the NMG and basic SISGS solvers, in Figure 4. The figure reveals not only the high efficiency of the FIM solvers, but also their generally steady residual

Figure 4: Convergence histories of various solvers for Couette flow on the uniform grid with  $N_1 = 512$ .Table 5: Iterations of the FIM-3 solver for Couette flow on various grids with  $\gamma_2 = 40, 300, 600$  for  $Kn = 0.1, 0.01, 0.001$ , respectively. The Ratio columns show the associated ratios between successive grids, with data for  $N_1 = 512$  taken from Table 4.

$N_1$	$Kn = 0.1, M = 9$		$Kn = 0.01, M = 7$		$Kn = 0.001, M = 5$	
	Iterations	Ratio	Iterations	Ratio	Iterations	Ratio
128	294	1.99	32	2.40	21	3.43
256	585	1.99	77	2.51	72	3.36

decay, except for the FIM-1 and FIM-2 solvers at  $Kn = 0.01$ , where some minor oscillations appear, attributable to instability induced by unoptimized choices of both the CFL number and  $\gamma_2$ . This increased instability at smaller  $Kn$  ultimately causes the FIM-1 solver to fail to converge at  $Kn = 0.001$ . However, owing to the implicit treatment of the collision term, both the FIM-2 and FIM-3 solvers continue to converge smoothly at  $Kn = 0.001$ , demonstrating their superior robustness.

The scaling behavior of the FIM solvers under grid refinement is then examined. Since the three FIM solvers exhibit nearly identical trends with respect to the grid number  $N_1$ , we present only the total number of iterations for the FIM-3 solver on two additional grids with  $N_1 = 128$  and  $256$  in Table 5, along with the associated iteration growth ratios between successive grid levels. It is observed that these growth ratios remain close to 2 at  $Kn = 0.1$ , and increase to around 3.4 at  $Kn = 0.001$ . By comparing these values with those listed in Table 3, we find that the FIM solvers share almost the same grid-dependent scaling behavior as the basic moment solvers across all three Knudsen numbers. In particular, although the growth ratio deteriorates as  $Kn$  decreases, the relative acceleration of the FIM solvers over the basic moment solvers is effectively preserved with negligible dependence on the grid, suggesting that their computational advantage is retained even as the grid is refined.

To further investigate the performance of the FIM solvers when used within the NMG framework, we take the NMG solver employing the FIM-3 solver for the smoother as a representative example. The total number of iterations and the corresponding wall-clock time, required by the NMG solver to reach the steady state on three grids with  $N_1 = 512, 1024$ , and  $2048$ , are reported in Table 6, of which the convergence histories, showing smooth and efficient residual decay for  $N_1 = 512$ , are illustrated in Figure 4. In all cases, convergence is achieved within a few dozen iterations, leading to an even more significant reduction in computational cost than the FIM-3 solver. Specifically, on the grid with  $N_1 = 512$ , the NMG solver consumes only about 14% of the wall-clock time required by the FIM-3 solver at  $Kn = 0.1$ . While the speedup becomes less pronounced at smaller  $Kn$ , the NMG solver still achieves a notable reduction in wall-clock time, with the ratio dropping to roughly 50% at both  $Kn = 0.01$  and  $0.001$ . This modest degradation in acceleration at smaller  $Kn$  is acceptable, considering that the FIM-3 solver itself already significantly outperforms the basic SISGS solver in these regimes. Actually, when comparing the NMG solver directly against the basic SISGS solver, the overall speedup becomes even more striking for all three  $Kn$ : on the grid with  $N_1 = 512$ , the NMG solver requires just about 1% of the wall-clock time consumed by the basic SISGS solver at  $Kn = 0.1$ ,

Table 6: Performance of the NMG solver for Couette flow, using FIM-3 as the smoother, on grids with  $N_1 = 512, 1024$ , and  $2048$ .  $T_r$ : wall-clock time ratio of NMG to FIM-3 with  $N_1 = 512$ .

$Kn$	$M$	Iterations			Wall-clock time (s)			$T_r$
		512	1024	2048	512	1024	2048	
0.1	10	27	40	61	61.06	179.55	546.82	13.8 %
	9	25	34	44	44.72	120.23	311.46	13.9 %
0.01	8	13	17	29	34.05	82.51	274.18	45.8 %
	7	12	16	24	27.14	65.79	197.00	44.9 %
0.001	6	18	28	42	54.69	187.32	566.01	52.5 %
	5	18	27	39	49.75	167.03	490.55	53.0 %

and this fraction drops even lower to approximately 0.35% at  $Kn = 0.01$  and 0.64% at  $Kn = 0.001$ .

As the grid is refined, the total number of iterations taken by the NMG solver increases moderately. To better illustrate this grid-dependent scaling behavior, Figure 5a plots the iteration growth trends with respect to the grid number  $N_1$  for both the NMG and FIM-3 solvers. Therein the numbers of iterations for the FIM-3 solver are normalized by  $N_t/5$ , where  $N_t$  denotes the number of iterations on the grid with  $N_1 = 128$ , as listed in the first row of Table 5. While the total number of iterations for the FIM-3 solver grows approximately linearly at  $Kn = 0.1$  and even superlinearly at smaller  $Kn$ , the growth exhibited by the NMG solver remains much lower and is further restrained on finer grids across all three cases. This contrast highlights the enhanced computational advantage of the NMG solver under grid refinement, with benefit becoming particularly pronounced at smaller Knudsen numbers.

As a supplement, we fix the order of the moment system at  $M = 5$  and display the wall-clock time consumed by the FIM-2, FIM-3, and NMG solvers, along with the basic SISGS solver, on the grid with  $N_1 = 512$  for varying Knudsen numbers in Figure 5b. It is reconfirmed that the basic SISGS solver incurs a considerable increase in computational cost with decreasing  $Kn$ , due to deteriorating convergence and the constant per-iteration cost. In contrast, with the help of the proposed FIM alternating iteration, the resulting solvers effectively suppress the computational cost across all tested  $Kn$ , leading to significantly improved efficiency. Although the acceleration effect of the FIM solvers becomes less noticeable at  $Kn = 0.1$ , their integration into the NMG framework still ensures overall efficiency comparable to that achieved at smaller  $Kn$ . Meanwhile, a slight rebound in wall-clock time is observed at  $Kn = 0.001$  for both the FIM and NMG solvers, suggesting that further optimization is necessary and potentially effective in this regime.

Finally, since higher-order moment systems contain more equations, basic moment solvers for them typically suffer from higher computational cost per iteration, often leading to a much longer overall runtime. However, the previous results reveal that the computational cost of FIM solvers can be effectively controlled even for a relatively high order  $M$  when  $Kn$  is small. This indicates that in the near-continuum flow regime, the FIM and FIM-based NMG solvers permit the use of moderately large  $M$  without incurring a substantial increase in wall-clock time, thereby offering greater flexibility in choosing  $M$  for practical applications.

**5.2. Shock structure.** The plane wave shock structure is another classical benchmark problem to test numerical methods for the Boltzmann equation [29, 13, 6]. The steady shock structure of Mach number  $Ma$  can be obtained by evolving a one-dimensional Riemann problem, where the initial condition is assumed to be a Maxwellian with the macroscopic quantities given on the left side  $x < 0$  by

$$(5.3) \quad \rho_l = 1.0, \quad \mathbf{u}_l = \left( \sqrt{5/3} Ma, 0, 0 \right)^T, \quad \theta_l = 1.0,$$

and on the right side  $x > 0$  by

$$(5.4) \quad \rho_r = \frac{4Ma^2}{Ma^2 + 3}, \quad \mathbf{u}_r = \left( \sqrt{\frac{5}{3}} \frac{Ma^2 + 3}{4Ma}, 0, 0 \right)^T, \quad \theta_r = \frac{5Ma^2 - 1}{4\rho_r}.$$

Numerically, the computational domain is taken as  $[-1.5, 1.5]$ , with boundary conditions imposed on each side according to the corresponding initial Maxwellian. To facilitate comparison with the experimental data



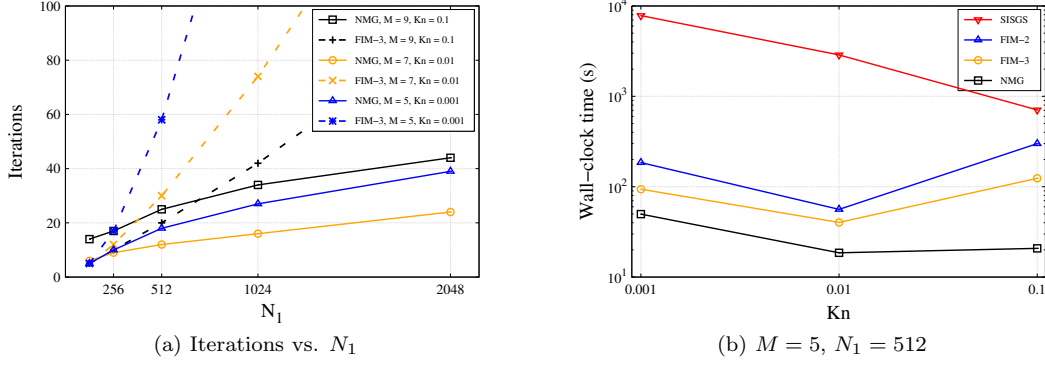


Figure 5: Performance of various solvers for Couette flow. The number of iterations for the FIM-3 solver is normalized by  $N_t/5$ , with  $N_t$  corresponding to the number of iterations for  $N_1 = 128$ , as given in Table 5.

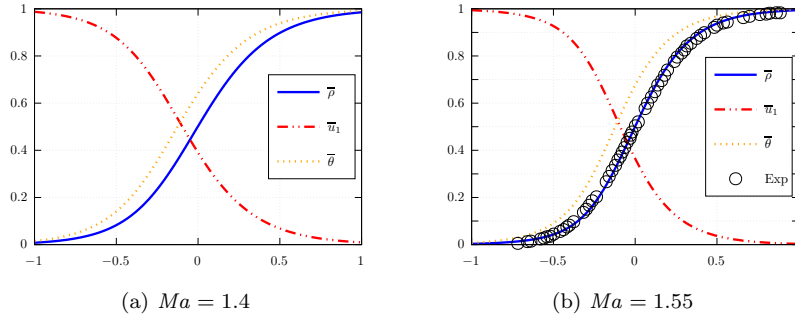


Figure 6: The shock structure for the moment system of order  $M = 7$  on the uniform grid with  $N_1 = 1024$ .

in [1], the collision frequency for the variable hard sphere model (see, e.g., [3]) is adopted as

$$(5.5) \quad \nu = \sqrt{\frac{2}{\pi}} \frac{(5 - 2\omega)(7 - 2\omega)}{15Kn} \rho \theta^{1-\omega}.$$

Consistent with the setup in [1, 13], we set the viscosity index to  $\omega = 0.72$  and the Knudsen number to  $Kn = 0.1$ . Below two Mach numbers  $Ma = 1.4$  and  $1.55$  are taken into account. For simplicity, the order of the moment system is fixed at  $M = 7$  and the convergence tolerance is chosen as  $Tol = 5 \times 10^{-5}$ .

The shock profiles computed on the grid with  $N_1 = 1024$  are shown in Figure 6, with the macroscopic quantities normalized as

$$(5.6) \quad \bar{\rho} = \frac{\rho - \rho_l}{\rho_r - \rho_l}, \quad \bar{u}_1 = \frac{u_1 - u_{1,r}}{u_{1,l} - u_{1,r}}, \quad \bar{\theta} = \frac{\theta - \theta_l}{\theta_r - \theta_l}.$$

As stated in [6], the moment system of order  $M = 7$  produces smooth shock structures for both Mach numbers, in good agreement with the experimental data.

The total number of iterations, along with the wall-clock time, consumed by the basic moment solvers and the FIM solvers on the grid with  $N_1 = 1024$ , are presented in Table 7, where the parameter  $\gamma_2$  in the FIM solvers is chosen as 5. It is observed that all of these solvers require somewhat more iterations at smaller  $Ma$ . For both Mach numbers, the forward Euler scheme and SIS exhibit nearly identical performance, converging in approximately the same number of iterations and consuming comparable wall-clock time as in the Couette flow tests. In contrast, the SISGS method greatly improves efficiency, with the total number of iterations reduced to roughly one-third and the wall-clock time to about half. A similar scaling trend is observed for the FIM solvers, which drastically reduce both the total number of iterations and wall-clock time to nearly 1/5 of those incurred by the corresponding basic moment solvers, resulting in a further remarkable gain

Table 7: Performance of basic moment and FIM solvers for shock structure computation with  $N_1 = 1024$  and  $\gamma_2 = 5$ .  $T_r$ : wall-clock time ratio of FIM-3 to SISGS.

$Ma$	Iterations			Wall-clock time (s)			
	Euler	SIS	SISGS	Euler	SIS	SISGS	
1.4	18153	18154	6589	3266.70	3250.31	1808.58	
1.55	16207	16210	5642	2907.08	2900.12	1550.99	
	FIM-1	FIM-2	FIM-3	FIM-1	FIM-2	FIM-3	$T_r$
1.4	3530	3534	1298	615.97	611.61	351.09	19.4%
1.55	3416	3420	1180	603.24	586.52	321.95	20.8%

Table 8: Performance of the NMG solver for shock structure computation under grid refinement, using FIM-3 as the smoother and fixing the coarsest grid to consist of 128 cells.  $T_r$ : wall-clock time ratio of NMG to FIM-3 with  $N_1 = 1024$ .

$Ma$	Iterations				Wall-clock time (s)				$T_r$
	1024	2048	4096	8192	1024	2048	4096	8192	
1.4	22	21	20	24	37.51	68.35	131.11	318.05	10.7 %
1.55	21	21	21	24	33.64	68.87	136.17	318.06	10.4 %

in efficiency, although the speedup appears slightly less impressive than that achieved in the Couette flow tests. While additional tests reveal that increasing  $\gamma_2$  generally leads to even faster convergence for the shock structure problem, albeit with a minor increase in instability risk, the current choice of  $\gamma_2 = 5$  already yields highly efficient performance, especially when the FIM solver is incorporated into the NMG framework.

In Table 8, the results of the NMG solver on four grids with  $N_1$  ranging from 1024 to 8192 are presented. Therein the FIM-3 solver is employed as the smoother, and the total number of grid levels is determined by fixing the coarsest grid to consist of 128 cells. Across all tests, convergence is achieved within 24 iterations, demonstrating excellent robustness and a further significant reduction in computational cost. Specifically, the wall-clock time on the grid with  $N_1 = 1024$  is only about 10% of that required by the FIM-3 solver on the same grid. Combined with the time ratio listed in Table 7, this indicates that the overall computational cost of the NMG solver is approximately 2.16% compared to that of the basic SISGS solver. Moreover, since the total number of iterations remains nearly independent of grid resolution, the efficiency gain becomes increasingly pronounced as the grid is refined.

Additionally, Figure 7 displays the convergence histories of the FIM, NMG and basic SISGS solvers with respect to wall-clock time, along with a comparison of their total wall-clock time. All FIM and NMG solvers exhibit steady and efficient residual decay, although a slight slowdown in convergence rate at later stages is observed for the FIM-1 and FIM-2 solvers. Notably, the NMG solver achieves the highest overall performance, characterized by a steepest residual decay with the lowest computational cost.

**5.3. Lid-driven cavity flow.** As one of the classical two-dimensional benchmark problems widely studied in the literature, the lid-driven cavity flow is taken as the third example. The same collision frequency as that given in (5.1) for the Couette flow is employed here. Following the setup explored in [14, 17, 19], we consider a square cavity of side length  $L = 1$  m with wall temperature  $T^W = 273$  K. The gas is initially in a uniform Maxwellian with constant density, mean velocity  $\mathbf{u}_0 = 0$  m/s, and temperature  $T_0 = T^W = 273$  K. As the top lid moves horizontally to the right at a constant speed  $u^W = 50$  m/s, the gas evolves and eventually reaches a steady state. Three initial densities, namely,  $\rho_0 = 8.58 \times 10^{-7}$  kg/m<sup>3</sup>,  $8.58 \times 10^{-6}$  kg/m<sup>3</sup>, and  $8.58 \times 10^{-5}$  kg/m<sup>3</sup>, corresponding to  $Kn = 0.1$ ,  $0.01$ , and  $0.001$ , respectively, are investigated below.

**5.3.1. Solution validation.** Similar to the Couette flow tests, we choose  $M = 9, 10$  for  $Kn = 0.1$ ,  $M = 7, 8$  for  $Kn = 0.01$ , and  $M = 5, 6$  for  $Kn = 0.001$  in our simulations. Numerical solutions on the

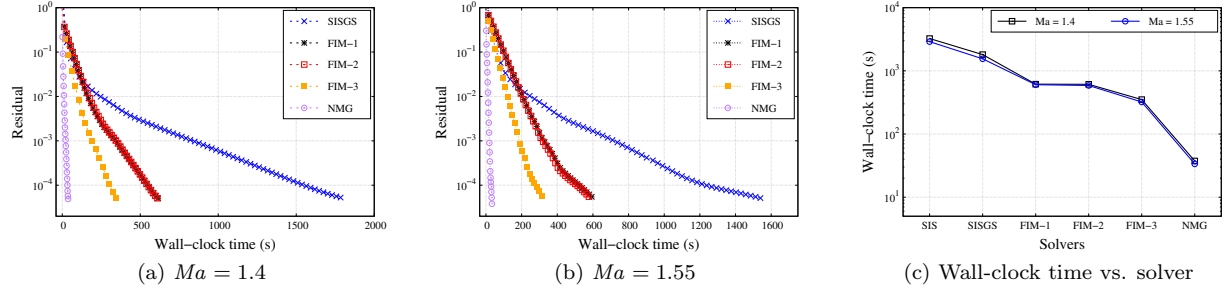


Figure 7: Convergence histories and computational costs of various solvers for shock structure computation on the uniform grid with  $N_1 = 1024$ .

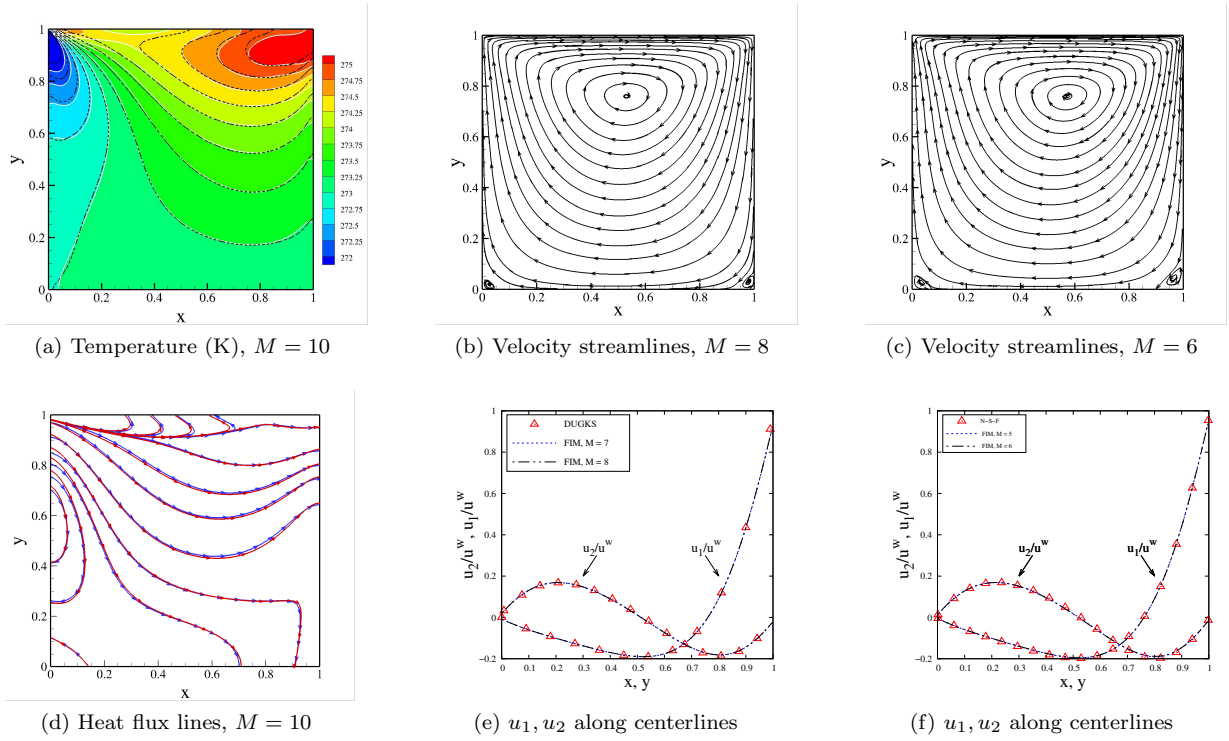


Figure 8: Numerical solutions of lid-driven cavity flow on the uniform  $512 \times 512$  grid. *Left column*: results at  $Kn = 0.1$ , with dashed and red lines denoting the reference DUGKS solutions; *Middle column*: velocity streamlines and normalized velocity profiles ( $u_1$  along the vertical centerline,  $u_2$  along the horizontal centerline) at  $Kn = 0.01$ ; *Right column*: corresponding velocity results at  $Kn = 0.001$ .

grid with  $N_1 = N_2 = 512$ , including the temperature field and heat flux streamlines at  $Kn = 0.1$ , and the velocity streamlines as well as normalized velocity profiles along the centerlines at both  $Kn = 0.01$  and  $0.001$ , are presented in Figure 8, where reference solutions are again obtained from the dugksFoam solver [31] for  $Kn = 0.1$  and  $0.01$ , and from the NSF equations for  $Kn = 0.001$ . These results show that the selected orders  $M$  are sufficient to produce solutions in close agreement with the references across all tested  $Kn$ , validating the capability of the moment system in the near-continuum flow regime using moderate orders.

**5.3.2. Solver performance.** The performance of the basic SIS and SISGS solvers, along with their associated FIM-2 and FIM-3 solvers, is first examined. Following several preliminary tests, as in the previous

Table 9: Performance of basic moment and FIM solvers for cavity flow with  $N_1 \times N_2 = 128 \times 128$  and  $\gamma_2 = 20, 100, 200$  for  $Kn = 0.1, 0.01, 0.001$ , respectively.  $T_r$ : wall-clock time ratio of FIM-3 to SISGS.

$Kn$	$M$	Iterations				Wall-clock time (s)				$T_r$
		SIS	FIM-2	SISGS	FIM-3	SIS	FIM-2	SISGS	FIM-3	
0.1	10	16154	1657	4737	529	86617.47	17813.71	38079.99	7983.22	21.0 %
	9	15606	1652	4525	517	64231.75	10591.34	28234.65	5860.41	20.8 %
0.01	8	25314	240	7328	92	79101.09	2798.35	35083.23	1897.88	5.4 %
	7	24229	232	6974	87	56033.27	1865.17	24735.46	1343.81	5.4 %
0.001	6	30826	196	9019	54	52382.96	1976.9	22863.31	1152.77	5.0 %
	5	29908	190	8696	52	35335.45	1626.77	15542.41	743.58	4.8 %

examples, the parameter  $\gamma_2$  in each FIM alternating iteration for the lid-driven cavity flow is set to 20, 100, and 200 for  $Kn = 0.1, 0.01$ , and  $0.001$ , respectively. The total number of iterations and wall-clock time, consumed by these solvers on the  $128 \times 128$  grid, are listed in Table 9.

It is observed that the basic SIS and SISGS solvers exhibit the main behavior analogous to that found in the one-dimensional tests. As  $Kn$  decreases toward  $0.001$ , both solvers experience a significant deterioration in convergence, while the basic SISGS solver maintains a nearly constant speedup over the SIS solver, with the wall-clock time reduced by more than half across all tested  $Kn$ . Consequently, at smaller  $Kn$ , their total numbers of iterations increase greatly, incurring considerable computational cost despite the use of lower-order moment systems. In contrast, the corresponding FIM solvers drastically reduce both the number of iterations and wall-clock time. This reduction becomes more pronounced as  $Kn$  decreases, resulting in a remarkable improvement in efficiency. For instance, the FIM-3 solver requires approximately 530 iterations to reach the steady state at  $Kn = 0.1$ , while this number drops sharply to about 90 at  $Kn = 0.01$ , and further to nearly 50 at  $Kn = 0.001$ . Accordingly, the wall-clock time of the FIM-3 solver relative to the basic SISGS solver decreases from around 20% at  $Kn = 0.1$ , to about 5% at both  $Kn = 0.01$  and  $0.001$ .

The NMG solver using the FIM-3 solver as the smoother is then evaluated. The results on three grids with  $N_1 \times N_2$  ranging from  $128 \times 128$  to  $512 \times 512$  are summarized in Table 10. In all cases, convergence is achieved within 30 iterations, indicating a substantial further reduction in computational cost, with the wall-clock time ratio of the NMG solver to the FIM-3 solver on the  $128 \times 128$  grid being about 15% at  $Kn = 0.1$  and around 50% at  $Kn = 0.01$ . By contrast, at  $Kn = 0.001$ , the NMG solver on the same grid requires only 7 iterations but consumes the wall-clock time comparable to that of the FIM-3 solver, offering no clear advantage. Nevertheless, this is not an intrinsic limitation, as the efficiency can still be effectively improved through appropriate tuning of the NMG parameters. Indeed, a supplemental test on this grid for the NMG solver shows that the wall-clock time decreases from 728 s listed in Table 10 for  $\gamma_2 = 200$  to around 400 s for a reduced  $\gamma_2 = 100$ , despite a slight growth in the total number of iterations.

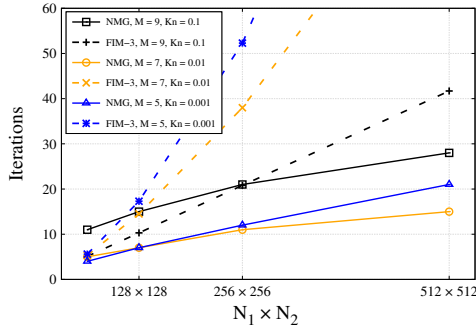
As the grid is refined, the total number of iterations incurred by the NMG solver increases somewhat faster than in the one-dimensional Couette flow tests. However, as illustrated in Figure 9a, this growth remains much slower than that of the FIM-3 solver, even at  $Kn = 0.001$ , where the total number of iterations for the NMG solver grows nearly linearly. Therefore, the efficiency advantage of the NMG solver is expected to persist and become increasingly significant on finer grids.

In addition, convergence histories of the FIM and NMG solvers, along with the basic SISGS solver, are plotted in terms of wall-clock time in Figure 10. Their computational cost versus  $Kn$  on the  $128 \times 128$  grid with  $M = 5$  is presented in Figure 9b. All results exhibit steady and efficient residual decay for the FIM and NMG solvers, demonstrating their robustness and superior efficiency. While the NMG solver is also observed to become less efficient as  $Kn$  decreases, and even to show little to no speedup over the FIM-3 solver at  $Kn = 0.001$ , it is worth reiterating that this shortcoming can be effectively mitigated by carefully optimizing the parameters in the solver.

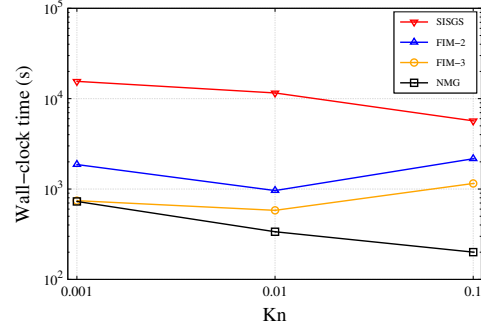
**6. Conclusion.** A novel fast iterative moment (FIM) method, which alternately solves the high-order moment system and the consistent hydrodynamic equations, has been developed for the steady-state Boltzmann-BGK equation. Benefiting from the use of the hydrodynamic equations to efficiently evolve the

Table 10: Performance of the NMG solver for cavity flow under grid refinement, using FIM-3 solver as the smoother.  $T_r$ : wall-clock time ratio of NMG to FIM-3 with  $N_1 \times N_2 = 128 \times 128$ .

$Kn$	$M$	Iterations			Wall-clock time (s)			$T_r$
		$128 \times 128$	$256 \times 256$	$512 \times 512$	$128 \times 128$	$256 \times 256$	$512 \times 512$	
0.1	10	16	22	30	1185.84	5086.56	24400.10	14.85 %
	9	15	21	28	839.69	3644.39	17495.09	14.33 %
0.01	8	8	12	16	966.76	4075.36	16483.24	50.94 %
	7	7	11	15	620.64	2971.82	13155.98	46.19 %
0.001	6	7	12	22	963.00	5420.30	34310.46	83.54 %
	5	7	12	21	728.63	4330.57	28040.09	97.99 %

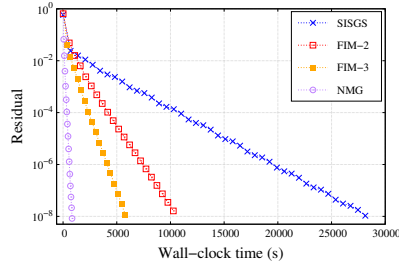


(a) Iterations vs. grid cells

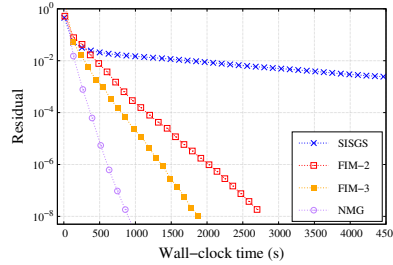


(b)  $M = 5$ ,  $N_1 = N_2 = 128$

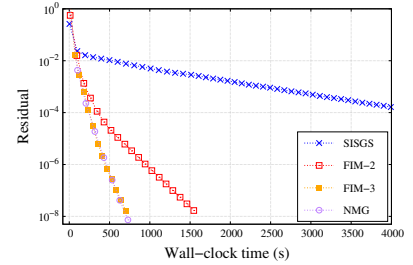
Figure 9: Performance of various solvers for cavity flow. The number of iterations for the FIM-3 solver is normalized by  $N_t = 50, 6$ , and  $3$  for  $Kn = 0.1, 0.01$ , and  $0.001$ , respectively.



(a)  $Kn = 0.1$ ,  $M = 9$



(b)  $Kn = 0.01$ ,  $M = 7$



(c)  $Kn = 0.001$ ,  $M = 5$

Figure 10: Convergence histories of various solvers for cavity flow on the uniform  $128 \times 128$  grid.

primary macroscopic quantities, the FIM method significantly accelerates convergence in the near-continuum flow regime, with such an acceleration becoming increasingly pronounced as  $Kn$  decreases. To improve robustness and efficiency, several targeted numerical strategies, including a semi-implicit scheme for the moment system and a symmetric Gauss-Seidel method for both the moment system and the hydrodynamic equations, have been incorporated into the FIM framework, yielding a family of FIM solvers with notably enhanced performance. It is also noteworthy that the present FIM method can be interpreted as a redesigned two-level NMLM method with improved robustness. Unlike the original NMLM method, however, this enhanced robustness enables the FIM method to be successfully incorporated into the spatial NMG framework, resulting in a more efficient multi-level solver that integrates coarse level corrections in both spatial and velocity spaces. Numerical experiments on planar Couette flow, shock structure, and two-dimensional lid-driven

cavity flow validate the effectiveness of the proposed FIM and FIM-based NMG solvers, confirming their robustness, efficiency and favorable scaling behavior in the near-continuum flow regime, particularly as  $Kn$  decreases or the grid is refined. Moreover, the FIM method allows for a flexible choice of order  $M$ , as the additional computational cost remains moderate even for a relatively high-order moment system.

Finally, to further enhance the performance of the FIM method, possible extensions, such as incorporating high-order spatial discretizations and Newton-type iterations, are currently under investigation and will be reported in forthcoming work.

## REFERENCES

- [1] H. ALSMEYER, *Density profiles in argon and nitrogen shock waves measured by the absorption of an electron beam*, J. Fluid Mech., 74 (1976), pp. 497–513.
- [2] P. L. BHATNAGAR, E. P. GROSS, AND M. KROOK, *A model for collision processes in gases. I. Small amplitude processes in charged and neutral one-component systems*, Phys. Rev., 94 (1954), pp. 511–525.
- [3] G. A. BIRD, *Molecular Gas Dynamics and the Direct Simulation of Gas Flows*, Oxford University Press, 1994.
- [4] S. BOSCARINO, S. Y. CHO, AND G. RUSSO, *A local velocity grid conservative semi-Lagrangian schemes for BGK model*, J. Comput. Phys., 460 (2022), p. 111178.
- [5] A. BRANDT AND O. E. LIVNE, *Multigrid Techniques: 1984 Guide with Applications to Fluid Dynamics*, Society for Industrial and Applied Mathematics, 2011.
- [6] Z. CAI, *Moment method as a numerical solver: Challenge from shock structure problems*, J. Comput. Phys., 444 (2021), p. 110593.
- [7] Z. CAI, X. DONG, AND J. HU, *Symmetric Gauss-Seidel method with a preconditioned fixed-point iteration for the steady-state Boltzmann equation*, 2024.
- [8] Z. CAI, Y. FAN, AND R. LI, *Globally hyperbolic regularization of Grad’s moment system*, Comm. Pure Appl. Math., 67 (2014), pp. 464–518.
- [9] Z. CAI, Y. FAN, AND R. LI, *A framework on moment model reduction for kinetic equation*, SIAM J. Appl. Math., 75 (2015), pp. 2001–2023.
- [10] Z. CAI AND R. LI, *Numerical regularized moment method of arbitrary order for Boltzmann-BGK equation*, SIAM J. Sci. Comput., 32 (2010), pp. 2875–2907.
- [11] Z. CAI, R. LI, AND Z. QIAO, *NRxx simulation of microflows with Shakhov model*, SIAM J. Sci. Comput., 34 (2012), pp. A339–A369.
- [12] Z. CAI, R. LI, AND Z. QIAO, *Globally hyperbolic regularized moment method with applications to microflow simulation*, Comput. & Fluids, 81 (2013), pp. 95–109.
- [13] Z. CAI, R. LI, AND Y. WANG, *Numerical regularized moment method for high Mach number flow*, Commun. Comput. Phys., 11 (2012), pp. 1415–1438.
- [14] Z. CAI AND M. TORRILHON, *Numerical simulation of microflows using moment methods with linearized collision operator*, J. Sci. Comput., 74 (2018), p. 336–374.
- [15] X. DONG AND Z. CAI, *Iterative methods of linearized moment equations for rarefied gases*, SIAM J. Sci. Comput., 46 (2024), pp. B669–B699.
- [16] H. GRAD, *On the kinetic theory of rarefied gases*, Comm. Pure Appl. Math., 2 (1949), pp. 331–407.
- [17] Z. HU, Z. CAI, AND Y. WANG, *Numerical simulation of microflows using Hermite spectral methods*, SIAM J. Sci. Comput., 42 (2020), pp. B105–B134.
- [18] Z. HU AND G. HU, *An efficient steady-state solver for microflows with high-order moment model*, J. Comput. Phys., 392 (2019), pp. 462–482.
- [19] Z. HU AND G. LI, *An efficient nonlinear multigrid solver for the simulation of rarefied gas cavity flow*, Commun. Comput. Phys., 34 (2023), pp. 357–391.
- [20] Z. HU AND R. LI, *A nonlinear multigrid steady-state solver for 1D microflow*, Comput. & Fluids, 103 (2014), pp. 193–203.
- [21] Z. HU, R. LI, AND Z. QIAO, *Acceleration for microflow simulations of high-order moment models by using lower-order model correction*, J. Comput. Phys., 327 (2016), pp. 225–244.
- [22] J. KOELLERMEIER AND H. VANDECASTEELE, *Hierarchical micro-macro acceleration for moment models of kinetic equations*, J. Comput. Phys., 488 (2023), p. 112194.
- [23] L. MIEUSSSENS, *Discrete velocity model and implicit scheme for the BGK equation of rarefied gas dynamics*, Math. Models Methods Appl. Sci., 10 (2000), pp. 1121–1149.
- [24] H. STRUCHTRUP, *Macroscopic Transport Equations for Rarefied Gas Flows: Approximation Methods in Kinetic Theory*, Springer-Verlag Berlin Heidelberg, 2005.
- [25] W. SU, L. ZHU, P. WANG, Y. ZHANG, AND L. WU, *Can we find steady-state solutions to multiscale rarefied gas flows within dozens of iterations?*, J. Comput. Phys., 407 (2020), p. 109245.
- [26] U. TROTTEBERG, C. W. OOSTERLEE, AND A. SCHULLER, *Multigrid*, Elsevier, 2000.
- [27] L. WU, *Rarefied Gas Dynamics: Kinetic Modeling and Multi-Scale Simulation*, Springer, 2022.
- [28] K. XU AND J.-C. HUANG, *A unified gas-kinetic scheme for continuum and rarefied flows*, J. Comput. Phys., 229 (2010), pp. 7747–7764.
- [29] K. XU AND J.-C. HUANG, *An improved unified gas-kinetic scheme and the study of shock structures*, IMA J. Appl. Math., 76 (2011), pp. 698–711.
- [30] L. M. YANG, C. SHU, J. WU, Y. Y. LIU, AND X. SHEN, *An efficient discrete velocity method with inner iteration for steady flows in all flow regimes*, Phys. Fluids, 34 (2022), p. 027110.

- [31] L. ZHU, S. CHEN, AND Z. GUO, *dugksFoam: An open source OpenFOAM solver for the Boltzmann model equation*, Comput. Phys. Commun., 213 (2017), pp. 155–164.
- [32] L. ZHU, X. PI, W. SU, Z.-H. LI, Y. ZHANG, AND L. WU, *General synthetic iterative scheme for nonlinear gas kinetic simulation of multi-scale rarefied gas flows*, J. Comput. Phys., 430 (2021), p. 110091.
- [33] Y. ZHU, C. ZHONG, AND K. XU, *Implicit unified gas-kinetic scheme for steady state solutions in all flow regimes*, J. Comput. Phys., 315 (2016), pp. 16–38.